Polyaniline-Grafted RuO$_2$-TiO$_2$ Heterostructure for the Catalysed Degradation of Methyl Orange in Darkness

Fatima Mousli [1,2,3,*], **Ahcène Chaouchi** [4], **Mohamed Jouini** [2], **François Maurel** [2], **Abdelaziz Kadri** [1] **and Mohamed M. Chehimi** [3,*]

[1] Laboratoire de Physique et Chimie des Matériaux (LPCM), Faculté des Sciences, Université Mouloud Mammeri, Tizi-Ouzou 15000, Algeria

[2] Sorbonne Paris Cité, Université Paris Diderot, CNRS, ITODYS (UMR 7086), 75013 Paris, France

[3] Université Paris Est, CNRS, ICMPE (UMR 7182), 94320 Thiais, France

[4] Laboratoire de Chimie Appliquée et Génie Chimique, Université Mouloud Mammeri, Tizi-Ouzou 15000, Algeria

[*] Correspondence: fatima.mousli@yahoo.fr (F.M.); chehimi@icmpe.cnrs.fr (M.M.C.)

check for updates

Abstract: Massive industrial and agricultural developments have led to adverse effects of environmental pollution resisting conventional treatment processes. The issue can be addressed via heterogeneous photocatalysis as witnessed recently. Herein, we have developed novel metal/semi-conductor/polymer nanocomposite for the catalyzed degradation and mineralization of a model organic dye pollutant in darkness. RuO$_2$-TiO$_2$ mixed oxide nanoparticles (NPs) were modified with diphenyl amino (DPA) groups from the 4-diphenylamine diazonium salt precursor. The latter was reduced with ascorbic acid to provide radicals that modified the NPs and further served for in situ synthesis of polyaniline (PANI) that resulted in RuO$_2$/TiO$_2$-DPA-PANI nanocomposite catalyst. Excellent adhesion of PANI to RuO$_2$/TiO$_2$-DPA was noted but not in the case of the bare mixed oxide. This stresses the central role of diazonium compounds to tether PANI to the underlying mixed oxide. RuO$_2$-TiO$_2$/DPA/PANI nanocomposite revealed superior catalytic properties in the degradation of Methyl Orange (MO) compared to RuO$_2$-TiO$_2$/PANI and RuO$_2$-TiO$_2$. Interestingly, it is active even in the darkness due to high PANI mass loading. In addition, PANI constitutes a protective layer of RuO$_2$-TiO$_2$ NPs that permitted us to reuse the RuO$_2$-TiO$_2$/DPA/PANI nanocomposite nine times, whereas RuO$_2$-TiO$_2$/PANI and RuO$_2$-TiO$_2$ were reused seven and five times only, respectively. The electronic displacements at the interface of the heterojunction metal/semi-conductor under visible light and the synergistic effects between PANI and RuO$_2$ result in the separation of electron-hole pairs and a reduction of its recombination rate as well as a significant catalytic activity of RuO$_2$-TiO$_2$/DPA/PANI under simulated sunlight and in the dark, respectively.

Keywords: RuO$_2$-TiO$_2$; diazonium salt; polyaniline; nanocomposite; catalysis; darkness

1. Introduction

The development of photocatalytic materials that are active both under visible light and in the dark constitute the subject of numerous studies targeted for environmental applications [1]. Since the last decade, titanium dioxide (TiO$_2$) has attracted much attention due to its great potential applications and its physico-chemical and catalytic properties [2–5]. It is a multifunctional semiconductor and one of the most promising materials for heterogeneous photocatalysis under UV irradiation. However, the use of TiO$_2$ is limited due to the high recombination rate of photoinduced electron-hole pairs produced during photocatalytic processes, few surface-active sites, light harvesting ability and the negligible absorbance

of visible light [6–9]. In this challenging context, efforts have been focused on the development of new materials with a lower electron-hole pair recombination rate and a strong absorption of sunlight. This involves combining the TiO_2 with another material that has a narrow band gap [10]. As a result, several TiO_2-based heterostructures have been designed in different forms such as: semiconductor n/semiconductor n: TiO_2-SnO_2 [11], TiO_2-WO_3 [12], TiO_2-ZnO [13], SiO_2-TiO_2 [14] semiconductor n/semiconductor p: TiO_2-Fe_2O_3 [15], TiO_2-Cu_2O [16], TiO_2-NiO [17] and noble metal/semiconductor n: Au-TiO_2 [18], Ag-TiO_2 [19], Pt-TiO_2 [20] Particularly, the metal/semiconductor n combination is widely investigated in various applications; the noble metals impart to the heterostructure a good electrocatalytic performance and super capacitive properties [21,22]. Among the numerous materials that could be combined with TiO_2 and serve to improve its catalytic performances, RuO_2 has raised much interest owing to its chemical and high thermal stability, low resistivity, high resistance to chemical corrosion, and its excellent diffusion properties make it an interesting material in numerous applications [23,24]. RuO_2 and TiO_2 have the same tetravalent cations; the different electron configurations between Ti and Ru create different physico-chemical properties in the oxides. TiO_2 is n-type semiconductor while RuO_2 has an electrical conductive metallic character [25] due to its partially filled metal (d)-oxygen (p) π^* band [26]. The combination between RuO_2 and TiO_2 or metal/semiconductor generally leads to the formation of the Schottky barrier which results in the improvement of the catalytic performances of the heterostructure, due to the difference in Fermi levels of the two materials [27]. Actually, the conductivity of TiO_2 increases owing to the presence of RuO_2 which favors the electronic exchange at the interface and thus increases the kinetics of the reactions in which it is involved [7]. It is noteworthy that a small percentage of RuO_2 relative to that of TiO_2 in the RuO_2-TiO_2 heterostructure (e.g., 10%) is sufficient to impart high conductivity, chemical and thermal stability and more importantly greater catalytic activity. This is an important economical aspect given the cost of ruthenium-based compounds. Due to these salient features, the conducting RuO_2-TiO_2 heterostructure is explored in the development of supercapacitors [23], electrode for chlorine electrogeneration [28] as well as pigments, fillers, electro-resistor films for electrodes, or dielectric device catalyst supports [29,30].

So far, and despite the above-mentioned interest of RuO_2-TiO_2 mixed oxide NPs, very few studies have been undertaken to evaluate their photocatalytic properties [7,23,24,31]. The catalytic activity of this heterostructure is related to the size of the particles, their morphology, and the specific surface area, which are dependent on the mode and the conditions of synthesis.

Several methods have been reported on the synthesis of RuO_2-TiO_2 in different forms. For example, Houšková et al. [32] prepared TiO_2 particles doped with RuO_2 by a hydrolysis process for the gas phase photodecomposition of acetone. Amama et al. [33] prepared this mixed oxide by impregnation for the photo-oxidation of trichloroethylene in aqueous medium. The majority of the research works are based on the synthesis of RuO_2-TiO_2 powders or films on plates of Ti or on other substrates by the sol gel route [23,27,34]. According to Panic et al. [35,36], anodes prepared by sol gel route have a considerably longer life service than those prepared by thermal decomposition. In addition, it is the most efficient approach for preparing nanoscale materials with a large specific surface area and important catalytic activity.

To enhance the electrical conductivity, the stability of (photo)catalysts and their photocatalytic efficiency, multiple cases of research were directed towards the design of TiO_2-based polymer nanocomposites. However, there are no reports on RuO_2-TiO_2/polymer nanocomposite catalysts, although TiO_2/polypyrrole [37] and TiO_2/polyaniline [38,39] were demonstrated to be efficient composite catalysts owing to the high absorption coefficient and a high mobility of charge carriers of TiO_2. These characteristics make it possible to improve the charge separation and therefore the catalytic performance of TiO_2-based catalytic materials [40]. Thus, there is room for investigating the design and catalytic properties of RuO_2-TiO_2/polymer nanocomposites. Indeed, recently we have revisited the design of TiO_2/polyaniline composite photocatalysts [41] by considering the mass loading of polyaniline (PANI) and its effect on the photocatalyst efficiency. To address this point, we have modified the

underlying TiO_2 NPs with aryl diazonium salts and found not only a much larger loading of PANI, but also made a remarkable recovery of the composite photocatalyst. Actually, diazonium salts emerged as versatile and efficient coupling or surface modifier agents of practically all types of materials (metals, semi-conductors, polymers, ceramics ...) [42]. Their use for surface functionalization is particularly interesting and easily applicable to nanomaterials [43] such as electrocatalysts [44] and photocatalysts [41]. In addition, and of relevance to this work, diazonium compounds act as unique coupling agents for polymers to surfaces [45,46]. Despite the remarkable performances achieved by grafting PANI to diphenylamine (DPA)-modified TiO_2, the final composite TiO_2-DPA-PANI was active under UV light only for the photocatalyzed degradation of Methyl Orange.

Returning to RuO_2-TiO_2 mixed oxide and its photocatalytic activity in the visible light, we reasoned that DPA modification would result in excellent adhesion of PANI and superior photoactivity under visible light conditions. In routine photocatalysis testing, all photocatalysts are actually incubated in the dark with the test solution of the model molecule to be degraded prior to exposure to UV or visible light. Surprisingly, RuO_2-TiO_2 mixed oxide NPs coated with PANI through a DPA aryl layer (hereafter, RuO_2-TiO_2/DPA/PANI), were found to completely degrade MO. This unpredicted result and thus good example of serendipity led us to conduct a thorough study on the catalytic properties of RuO_2-TiO_2/DPA/PANI under dark and to compare the catalytic properties to those of bare RuO_2-TiO_2 mixed oxide and RuO_2-TiO_2/PANI.

In this work, RuO_2-TiO_2 mixed oxide NPs were prepared and modified with aryl diazonium compounds from the diphenylamine precursor and subsequently grafted with in situ prepared polyaniline. The final nanocomposite, denoted RuO_2-TiO_2/DPA/PANI, was evaluated as a nanocatalyst of the degradation of Methyl Orange taken as a model organic pollutant. To highlight the role of both the diazonium modification step and the importance of polyaniline in the performances of the nanocomposite catalyst, the following reference compounds were also prepared and tested: pristine RuO_2-TiO_2 and RuO_2-TiO_2/PANI nanoparticles. The RuO_2-TiO_2/DPA/PANI nanocomposite and related materials were thoroughly characterized by infrared and Raman spectroscopy, SEM/EDS, UV-Vis, XRD, TGA and XPS. The photocatalytic performances were investigated under dark and under simulated sunlight. The extent of residual Methyl Orange after catalyzed reaction was determined by UV-vis spectroscopy.

Whilst much has been said about TiO_2 and TiO_2-based mixed oxide photocatalysts, to the very best of our knowledge:

(i) no work has been undertaken on the combination of RuO_2-TiO_2 mixed oxide with conductive polymers,

(ii) no strategy has been reported so far to take advantage of the synergetic effects of surface functionalization of RuO_2-TiO_2 using diazonium salts and post grafting with conductive polymers in view of making a new generation of (photo)catalysts.

By combining the best of two worlds: *ca* visible light active RuO_2-TiO_2 photocatalysts and diazonium coupling agents for the attachment of conductive polymers able of charge transfer, we offer unique heterostructure with catalytic activity under darkness. This is what has motivated this in-depth study.

2. Results and Discussion

2.1. General Strategy of Designing RuO_2-TiO_2/PANI Nanocomposites

RuO_2-TiO_2/PANI nanocomposites were prepared in four steps: (i) sol-gel synthesis of TiO_2 followed by (ii) RuO_2 doping (via sol-gel method), then the mixed oxide was (iii) grafted with DPA aryl nano-layer from diazonium precursor; (iv) the RuO_2-TiO_2/DPA served as substrates for the in situ synthesis of PANI. It is to note that the sol-gel route for the mixed oxide was selected due to its simplicity and the preparation of the catalyst in high yield.

Figure 1 schematically displays the general pathway of making RuO_2-TiO_2/PANI nanocomposites (Figure 1A, upper panel) and digital photographs of the different materials prepared (Figure 1B, lower panel). First, the nanoparticles of RuO_2-TiO_2 mixed oxide were functionalized with isolated 4-diphenylamine diazonium tetrafluoroborate at 0 °C in the presence of the diazonium reducing agent vitamin C. The DPA layer formed on the surface of RuO_2-TiO_2 NPS acts as surface-attached initiator for the in situ oxidative polymerization of aniline. It was necessary to prepare the RuO_2-TiO_2/PANI nanocomposite by polymerizing the aniline monomer under the same conditions on the surface of the pristine mixed oxide NPs in order to account for the role of DPA as a coupling agent.

Figure 1B shows digital photographs of the main samples, pristine (Ba) and modified (Bb, Bc, Bd). The functionalization of RuO_2-TiO_2 mixed oxide nanopowders with diazonium salt is manifested by a change in color from dark gray to pale green (Figure 1Bb). A slight, even negligible change in color has been observed for RuO_2-TiO_2/PANI nanocomposite, despite the striking color of PANI (Figure 1Bc). The gray color of the RuO_2-TiO_2 nanoparticles is no longer visible by observing the nanopowders of RuO_2-TiO_2/DPA/PANI, the dark green color of the PANI covers all the RuO_2-TiO_2 powder previously modified with DPA (Figure 1Bd). This reflects the spectacular role of DPA salt in the process of polymerization of the polymer on the surface of RuO_2-TiO_2 heterojunction, as well as its effect on the optical properties of the nanocomposite formed.
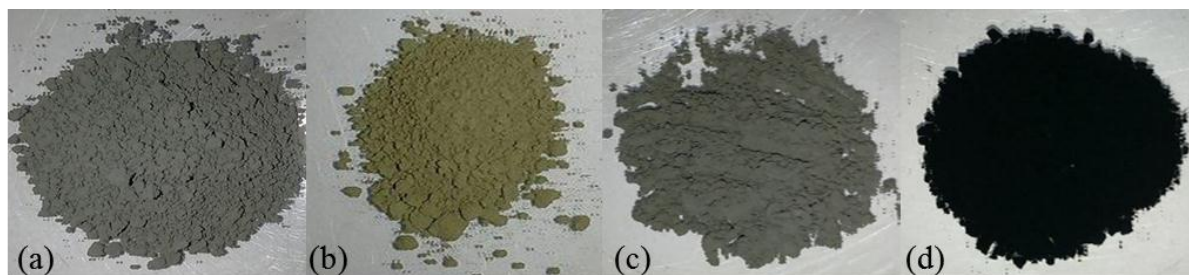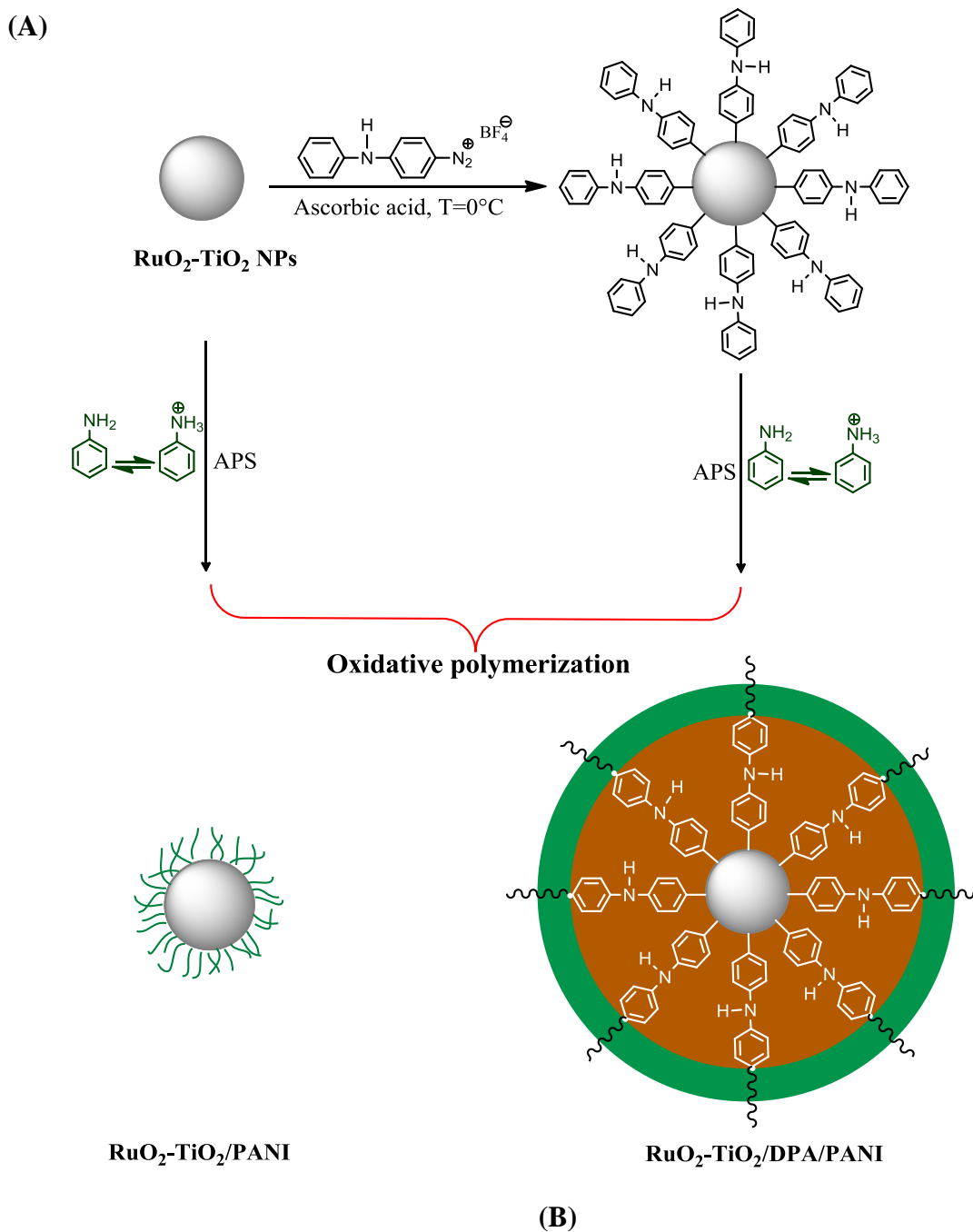
(A)

(B)

Figure 1. Synthesis of RuO$_2$-TiO$_2$/PANI nanocomposite (Upper panel: Figure 1**A**) and digital photographs of pristine RuO$_2$-TiO$_2$ (a), RuO$_2$-TiO$_2$-DPA (b), RuO$_2$-TiO$_2$-PANI (c), and RuO$_2$-TiO$_2$-DPA-PANI (d) (Lower panel: Figure 1**B**).

2.2. *RuO₂-TiO₂ Characterization*

2.2.1. Point of Zero Charge (PZC) of RuO$_2$-TiO$_2$ by Zeta Potential Measurement

The Point of zero charge (PZC) is the pH at which the surface of a particle is electrically neutral [47]. Figure 2 depicts the evolution of the zeta potential in the pH ranging from 1.5 to 13 for RuO$_2$-TiO$_2$ heterojunction NPs. The plot shows that the PZC of the RuO$_2$-TiO$_2$ heterostructure is 5.8. The value of PZC of RuO$_2$-TiO$_2$ NPs decreased compared to those of TiO$_2$ anatase reported in the literature. Li et al. [48] have marked the PZC for pure TiO$_2$ anatase at pH = 7, this result is similar to that found by Song et al. [49]. Uchikoshi [50] reported another value which is about 6.7. These values remain dependent on the working conditions namely the measuring device, the electrolyte support and the nature of the material.
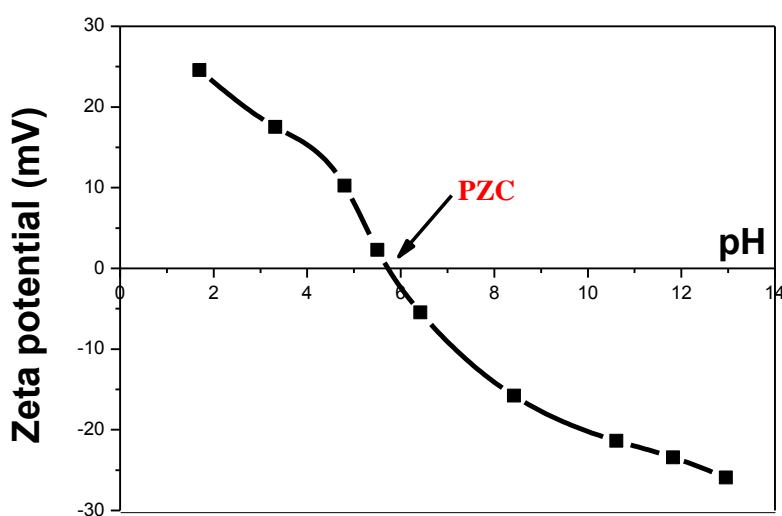

Figure 2. Variation of the zeta potential of RuO$_2$-TiO$_2$ NPs dispersed in NaCl as a function of the pH.

2.2.2. Dielectric Characterization

Electrical impedance spectroscopy has been widely used to study the charge transport behavior of nanocrystalline materials, providing information on the electrical and structural properties of materials. For a detailed study of charge transport properties of RuO$_2$-TiO$_2$ mixed oxide nanoparticles as a function of temperature, the impedance measurements were carried out in the frequency region from 100 Hz to 1 MHz. The electrical properties of the RuO$_2$-TiO$_2$ heterojunction have not yet been studied. The combination of ruthenium oxide with a metallic character and titanium dioxide semiconductor (n) generates original electrical characteristics different from those of simple and spinel oxides.

Figure 3a,b display the variation of the real part (Z') and imagines part (Z'') of impedance versus frequency (10^3 to 10^6 Hz) at different temperatures. The plots show a sigmoidal variation as a function of frequency in the low frequency region followed by saturation in the high frequency region. These results represent the mixed nature of polarization behavior in the material. The converge of all Z' and Z'' curves at high frequency indicates a possibility of the release space charge in the RuO$_2$-TiO$_2$ material, as a result of lowering in the barrier properties of the material. The curves indicate that the electrical conduction increases with rise in temperature, this variation depends on the release of the space charge. In the low frequency region, a very strong dependence of the impedance of the material as a function of frequency and temperature has been recorded, this may be related to a change in the charge order model under the effect of temperature; this effect shows also a noticeable change in its behavior in the low frequency region. A decreasing trend of Z' temperature rise suggests the presence of negative temperature coefficient of resistance (NTCR) in the material in the low frequency region, but tends to merge in the high frequency region at almost all temperatures. These results indicate a

possibility of increase in alternating current (ac) conductivity with increasing temperature in the high frequency region, possibly due to the release of space charge.
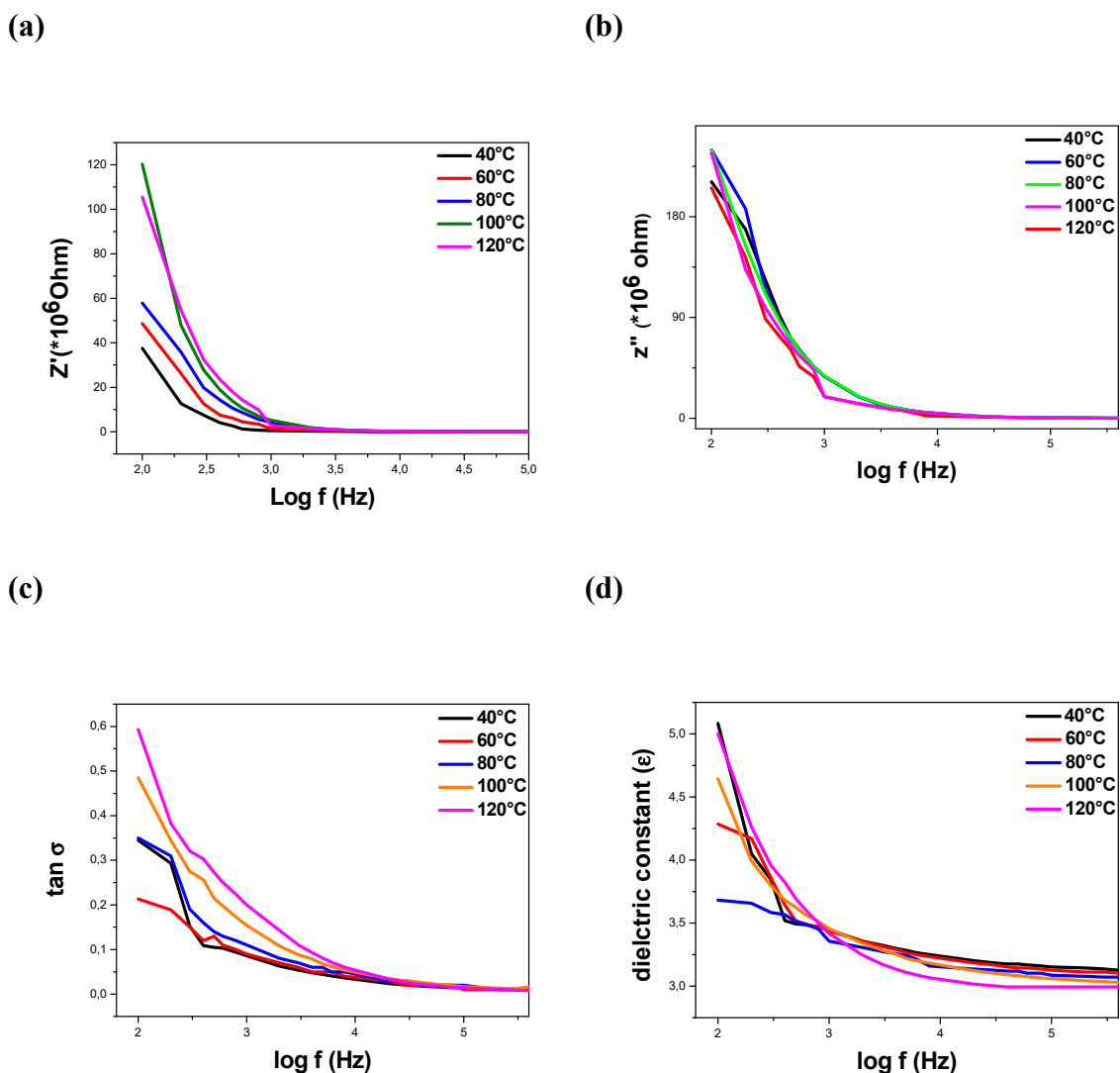
(a)　　　　　　　　　　　　　　　　　　　　**(b)**

(c)　　　　　　　　　　　　　　　　　　　　**(d)**

Figure 3. Frequency dependence of (**a**) Z′, (**b**) Z″, (**c**) relative dielectric permittivity and (**d**) imaginary part of the relative dielectric permittivity.

Figure 3c shows the frequency dependence of the relative dielectric permittivity of RuO_2-TiO_2 sample at different temperature and frequency. The dependent dielectric permittivity of the RuO_2-TiO_2 material decreases with increasing of temperature and frequency. This phenomenon can be attributed to the different dipole orientations by charge carriers bounded at different localized states [51,52]. The electron can hop between a pair of these centers under the action of an alternating current field, leading to the reorientation of an electric dipole. This process conducted to a change in the dielectric permittivity. Therefore, the increase in the dielectric permittivity with decreasing frequency can be attributed presence of the space charges in the material [53].

Figure 3d displays the frequency dependence of the imaginary part of the relative dielectric permittivity of RuO_2-TiO_2 at various temperatures and frequencies. The curves show that the imaginary part of the relative dielectric permittivity increased with increasing temperature. However, the imaginary part of the relative dielectric permittivity decreased as the frequency increased. As high frequency, the imaginary part of the relative dielectric permittivity measured at different temperature ranges converge to similar values. This is probably due to the small value of the conductance compared

with the rapidly increased angular frequency ranges. Usually metal oxide materials can be expressed n-type semiconductor due to their oxygen vacancies, therefore free electrons from the metal sites can be easily released by high temperature; so, the imaginary part of relative dielectric permittivity has closed relationship with the conductance. As a result, the imaginary part of relative dielectric permittivity of RuO_2-TiO_2 composition at the high temperature near the low frequency has high values.

2.3. Characterization of RuO₂-TiO₂/PANI Nanocomposites

2.3.1. Resistivity by Four Point Probe Measurements

During the catalytic processes, the electrons which are on the surface interact during the whole time of the catalyzed reaction inducing the formation of an electric current. It is therefore possible to correlate the catalytic efficiency of solid catalysts by measuring the electronic conductivity within the materials.

The resistivity of material can be determined using Four Point Probe method and calculated by applying the following relation:

$$R = \frac{V}{I} = K \cdot \frac{\rho}{e}$$

where: R is the resistance (Ω), ρ the resistivity ($\Omega.\ m$), e the thickness of the pellet (cm) and K the dimensionless coefficient characteristic of 2D geometry (shape of contours, position of contacts).

$$K = \frac{Ln\ 2}{\pi} \quad \frac{1}{K} = 4.532 \quad \rho = \frac{V \times e \times \pi}{I \times Ln2}$$

The conductivity is given by:

$$\sigma = \frac{1}{\rho}$$

Table 1 summarizes the results obtained for the various catalysts at similar pellet thickness.

Table 1. Conductivity and resistivity of pure TiO_2 and RuO_2-TiO_2-based nanocatalysts.

Materials	e (cm)	R (Ω)	ρ ($\Omega.$ cm)	σ (S/cm)
TiO_2	0.20	0.0119	0.0109	91.7
RuO_2-TiO_2	0.23	0.0030	0.0032	317
PANI	0.21	0.0111	0.0106	94
RuO_2-TiO_2/PANI	0.23	0.0028	0.003	343
RuO_2-TiO_2/DPA/PANI	0.24	0.0024	0.0026	384

The resistivity of the RuO_2-TiO_2 heterostructure and related materials was studied on compressed materials pellets by setting a current of 0.1 mA at room temperature. The results highlight the effect of RuO_2 on the conductivity of RuO_2-TiO_2 NPs by comparing the results obtained with those of pure TiO_2, as well as the effect of PANI on the conductivity of nanocomposites by comparing pure RuO_2-TiO_2 NPs.

Ruthenium dioxide is widely known for its low resistivity and high conductivity which has allowed it to be ranked among the best conductive oxides at room temperature [54–56]. As a result, the resistivity of RuO_2-TiO_2 heterojunction is three times lower than that of pure TiO_2, the results showed also that the conductivity of the mixed oxide RuO_2-TiO_2 is much higher than that recorded for TiO_2; this reveals that the combination between RuO_2 and TiO_2 leads to the formation of a new material with interesting electric properties.

The presence of PANI on the surface of RuO_2-TiO_2 has a significant effect on the electrical conductivity of the final nanocomposites. Cao et al. [57] were the first to obtain PANI films with a high electrical conductivity greater than 10^2 S/cm. The PANI present on the surface of RuO_2-TiO_2 is doped with SO_4^{2-} at 50% and the measured conductivity is 94 S/cm. The results reveal that the conductivity of

the nanocomposites obtained increases with the increase of the amount of PANI; it's worth 343 and 384 S/cm for RuO_2-TiO_2/PANI and RuO_2-TiO_2/DPA/PANI respectively.

The conductivity and the resistivity of materials are controlled by the number of free electrons and/or their mobility. As a matter of fact, the mobility of electrons increases with the increase of grain size [58], which is the case in this study.

2.3.2. X-Ray Diffraction

XRD was used to identify the different crystalline phases containing the samples of the heterostructure RuO_2-TiO_2 NPs, RuO_2-TiO_2/DPA, RuO_2-TiO_2/PANI and RuO_2-TiO_2/DPA/PANI nanocomposite. The pattern of RuO_2-TiO_2 NPs (Figure 4a) obtained in the range $65° \geq 2\theta \geq 20°$ confirms the formation of the mixed oxide and the total conversion of $RuCl_3$ into RuO_2. It exhibits the different peaks expected for TiO_2 in its anatase form: $2\theta = 25.4°$, $37.1°$, $37.79°$, $53.8°$, $55.2°$, $62.9°$ and $70.06°$ related to TiO_2 reflections in planes (101), (103), (004), (105), (200), (204) and (220) respectively, and those of RuO_2 rutile: $2\theta = 28.1°$, $35°$, $40.1°$, $40.8°$, 45.3, $59.6°$ and $69.6°$ corresponding to RuO_2 reflections in planes (110), (101), (200), (111), (210), (002) and (301), respectively. The intensity of peaks corresponding to RuO_2 is low compared to that recorded for peaks of TiO_2, which means that titanium oxide is predominant. The crystallite size estimated using Scherer's formula for each oxide, calculated from the broadening of their most intense dispersion bands (TiO_2: (101), RuO_2: (110)) is 6.5 nm for TiO_2 and 8.7 nm for RuO_2.
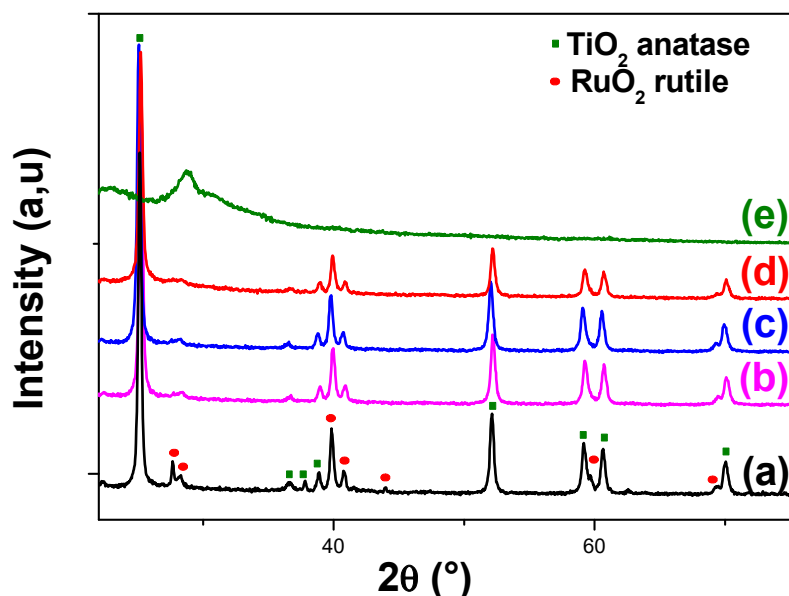

Figure 4. XRD patterns of RuO_2-TiO_2 NPs (**a**), RuO_2-TiO_2/DPA (**b**), RuO_2-TiO_2/PANI (**c**), RuO_2-TiO_2/ DPA/PANI (**d**) and PANI (**e**).

The diffraction spectra of RuO_2-TiO_2 after modification with diazonium salt and PANI reveal the expected peaks of pristine RuO_2-TiO_2. No new phase was detected, however, the peaks located at $28.12°$, $37.79°$, $45.31°$ and $59.6°$ characteristics of RuO_2-TiO_2 NPs do not appear on the spectra (b), (c) and (d) corresponding to RuO_2-TiO_2/DPA, RuO_2-TiO_2/PANI and RuO_2-TiO_2/DPA/PANI. No other peaks corresponding to the diazonium salt appeared on the spectra, it is noted that the X-ray diffraction does not detect non-crystalline organic matter.

2.3.3. UV-vis

Figure 5 displays UV-vis spectra of the samples recorded in the wave range 200–800 nm. The spectrum of RuO_2-TiO_2 NPs is marked by the presence of lower intensity TiO_2 absorption bands

centered at 200 and 350 nm. Furthermore, there are broad bands between 400 and 600 nm corresponding to RuO_2; these bands are characterized by a high intensity which is due to the strong absorption of RuO_2. The width of these bands is probably due to the charge transfer between oxygen and ruthenium [59]. The absorption of visible light by the mixed oxide RuO_2-TiO_2 can be attributed to the external effect of resonance that is related to the excitation of electron collective oscillations in the RuO_2 nanoparticles by the electric field of the electromagnetic wave [60].
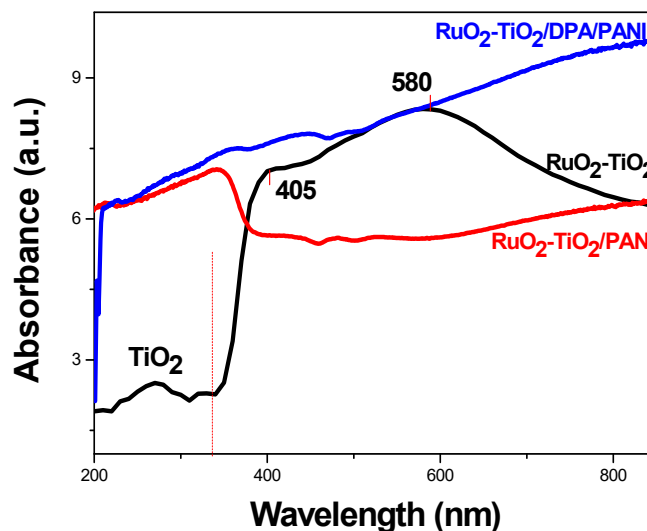

Figure 5. UV-vis spectra of RuO_2-TiO_2 NPs, RuO_2-TiO_2/PANI and RuO_2-TiO_2/DPA/PANI nanocomposite.

The band gap energy (Eg) of the RuO_2-TiO_2 heterostructure was calculated from the UV-vis spectrum applying the following equation:

$$\alpha(h\upsilon) = A(h\upsilon - Eg)^n$$

where α: absorption coefficient, υ: light frequency, Eg: band gap energy and A: constant. (n) is determined by the type of optical transition of semiconductor (n = 1/2 or n = 2 for direct or indirect transition). Therefore, the band gap energy calculated for RuO_2-TiO_2 heterojunction from the $(\alpha h\upsilon)^n = f(h\upsilon)$ plot was 2.7 eV for indirect transition and 3.19 eV for direct transition.

PANI has high absorption in the UV as well as in the visible light [61]. Compared to RuO_2-TiO_2 NPs, the TiO_2 absorbance in the RuO_2-TiO_2/PANI nanocomposite increased significantly in the visible range while that of the RuO_2 decreased in the UV. This indicates that the presence of PANI even in small amounts has extended the absorption of TiO_2 to the range of visible light [61]. The RuO_2-TiO_2/DPA/PANI nanocomposite has the same optical properties as the PANI; the corresponding spectrum is almost similar to that of the polyaniline represented in the literature [61,62]. The spectrum reveals the increase of the absorbance with the appearance of a small wave between 469 and 510 nm, corresponding to the π-π^* transition in the polymeric chain [63]. The increase in the absorption of the two nanocomposites is due to the delocalization of the carrier's n-π^* [64].

2.3.4. Infrared Spectroscopy

Figure 6 displays superimposed spectra of RuO_2-TiO_2/DPA/PANI and related compounds. The spectrum of pristine RuO_2-TiO_2 NPs (Figure 6a) presents two characteristic bands of titanium dioxide located at 432 and 815 cm^{-1} attributed to Ti=O and Ti-O-Ti stretching vibrations, respectively. The band centered at 690 cm^{-1} accounts for the vibration of Ru-O and deformation of Ru-O–H [65]. Uddin et al. [7] did not obtain any band corresponding to RuO_2 in their IR study of RuO_2-TiO_2 mixed oxide and the spectrum they have displayed was similar to that of pure TiO_2. The spectrum

of DPA diazonium (Figure 6b) is marked by bands centered at 1580 cm^{-1} and 1610 cm^{-1} which correspond to the aromatic C=C stretching, a signal has been recorded around 1180 cm^{-1} which is assigned to C–H benzene ring stretching band [66]. The spectrum shows the characteristic bands of diazonium salt at 3340 and 2232 cm^{-1} corresponding to the N–H and N≡N stretching mode of diazonium salt, respectively. Particularly, the characteristic N≡N band does not appear in the spectrum of RuO$_2$-TiO$_2$/DPA (Figure 6c) which confirms the attachment of aryl layer by diazonization of the parent diazonium salt [67]. The spectrum of the RuO$_2$-TiO$_2$/PANI nanocomposite (Figure 6e), is almost similar to that of the pristine mixed oxide except three bands belonging to the PANI vibrational result, a band at 1232 cm^{-1} is ascribed to C–N stretching vibration. That located at 1400 cm^{-1} is relative to C=C aromatic ring stretching of the benzenoid vibration. An intense peak appeared around 1126 cm^{-1} attributed to C–H in-plane deformation [68]. The analysis of the RuO$_2$-TiO$_2$/DPA/PANI sample (Figure 6f) showed the same features as pure PANI (Figure 6d), all bonds detected belong to the polymer. In addition to the bands present on the RuO$_2$-TiO$_2$/PANI nanocomposite spectrum, a band at about 1565 cm^{-1} is lumped with C=C stretching of quinoid vibration [69]. This result means that the RuO$_2$-TiO$_2$/DPA surface is totally covered by PANI.
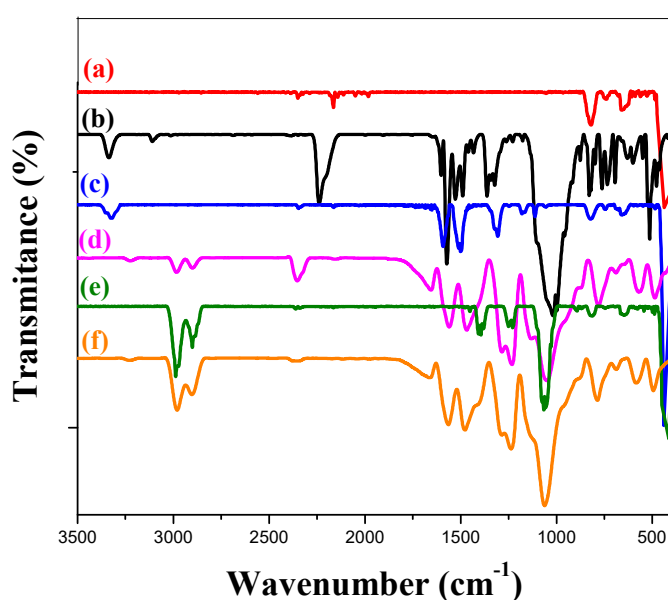

Figure 6. FTIR absorption spectra of (**a**): RuO$_2$-TiO$_2$, (**b**): DPA, (**c**): RuO$_2$-TiO$_2$/DPA, (**d**): PANI, (**e**): RuO$_2$-TiO$_2$/PANI and (**f**): RuO$_2$-TiO$_2$/DPA/PANI.

2.3.5. Raman

Ruthenium dioxide in rutile phase has a tetragonal structure with two molecules of RuO$_2$ per unit cell; it has 15 modes of optical phonons, three of which are Raman-active in the 400–800 cm^{-1} range with the symmetries E$_g$ corresponding to a doublet as well as A$_{1g}$ and B$_{2g}$ which are singlets [70]. Several studies have already shown that the TiO$_2$ anatase is usually manifested with Raman-active modes that are E$_g$ (144 cm^{-1}), E$_g$ (197 cm^{-1}), B$_{1g}$ (399 cm^{-1}), A$_{1g}$ (514 cm^{-1}), B$_{1g}$ (514 cm^{-1}) and E$_g$ (639 cm^{-1}) [71]. The RuO$_2$-TiO$_2$ heterostructure is a combination of Rutile RuO$_2$ and TiO$_2$ anatase which could be distinguished by their Raman-active modes on the same spectrum. Figure 7 displays superimposed Raman spectra of RuO$_2$-TiO$_2$ NPs, pure PANI and their reference materials. The spectrum of pristine RuO$_2$-TiO$_2$ NPs (Figure 7a) shows three distinct peaks located at 528, 646 and 716 cm^{-1} assigned to E$_g$, A$_{1g}$ and B$_{2g}$ phonons vibrations respectively corresponding to ruthenium oxide in the rutile phase, these bands are in agreement with those reported in the literature [72]. The spectrum shows also another band at 197 cm^{-1} attributed to the vibration mode E$_g$ specific to TiO$_2$ anatase.
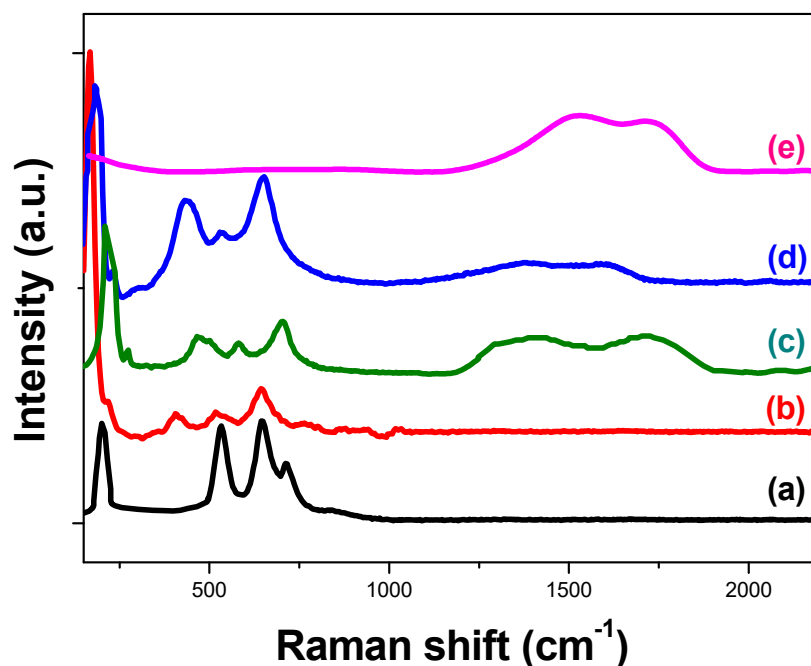
Figure 7. Raman spectra of pristine RuO_2-TiO_2 NPs (**a**), RuO_2-TiO_2/DPA (**b**), RuO_2-TiO_2/PANI (**c**), RuO_2-TiO_2/DPA/PANI (**d**) and PANI (**e**).

The spectrum of DPA-modified RuO_2-TiO_2 NPS shows a very remarkable red shift of RuO_2-TiO_2 characteristic bands, which confirms the grafting of DPA on the surface of the heterostructure (Figure 7b). It is noted that the Raman shift is a difference in atomic weight between pure RuO_2-TiO_2 and RuO_2-TiO_2/DPA.

The polymerization of PANI on RuO_2-TiO_2 NPs surface did not lead to the displacement of the Raman bonds of the nanoparticles, but to a slight broadening of the latter and a vibrational response recorded between 1200 and 1800 cm^{-1} which corresponds to the polymer (Figure 7c). The spectrum of RuO_2-TiO_2/DPA/PANI nanocomposite shows an increase in the baseline comparing with RuO_2-TiO_2 and RuO_2-TiO_2/DPA curves. An increase in the intensity and a considerable broadening of the bands have been registered, in addition to the shift of the characteristic bands of PANI toward lower; this can be explained by the insertion of a large amount of organic matter, *ca.* PANI in the actual case (Figure 7d).

2.3.6. Thermogravimetric Analysis (TGA)

The mass loading of organics attached on the surface of RuO_2-TiO_2 heterostructure NPs was determined using TGA carried under air flow. Pristine RuO_2-TiO_2 mixed oxide and DPA-modified RuO_2-TiO_2 exhibit a thermal stability up to 800 °C (Figure 8a,c). The weight loss is negligible; it is 1% for RuO_2-TiO_2 bare and 1.5% for RuO_2-TiO_2/PANI which could be caused by the evaporation of H_2O molecules adsorbed on the surface (Figure 8a,b). The quantity of organic matter loaded on the surface of RuO_2-TiO_2 heterostructure was determined according to the weight loss, it was 1.52% of PANI, and 9.8% of DPA. In the case of RuO_2-TiO_2/DPA/PANI, the weight loss is as high as 27.8% for the aryl and PANI layers. These results confirm the role of DPA as a coupling agent for the polymer on the RuO_2-TiO_2 NPs surface. The thermal degradation of RuO_2-TiO_2/PANI and RuO_2-TiO_2/DPA/PANI nanocomposite occurs in two steps: the reduction of the initial mass of the samples in the temperature range between 50 and 230 °C which can be attributed to the removal of H_2O molecules adsorbed on the surface of the particles. The second step between 230 and 800 °C, assigned to the thermal decomposition of the inserted polyaniline chains (Figure 8b,d). The total thermal decomposition of the polymer on the unmodified RuO_2-TiO_2 surface occurred at temperatures above 600 °C while for

the RuO$_2$-TiO$_2$/DPA/PANI nanocomposite, the total decomposition of PANI occurred at temperatures raised above 800 °C; this is probably due to the diazonium salt, which seems to have a retarding effect on the decomposition of the polymeric chains. The addition of DPA has strengthened the bonds between RuO$_2$-TiO$_2$ nanoparticles and PANI and the increase of the interaction between these two elements led to the formation of a highly temperature-resistant composite material.
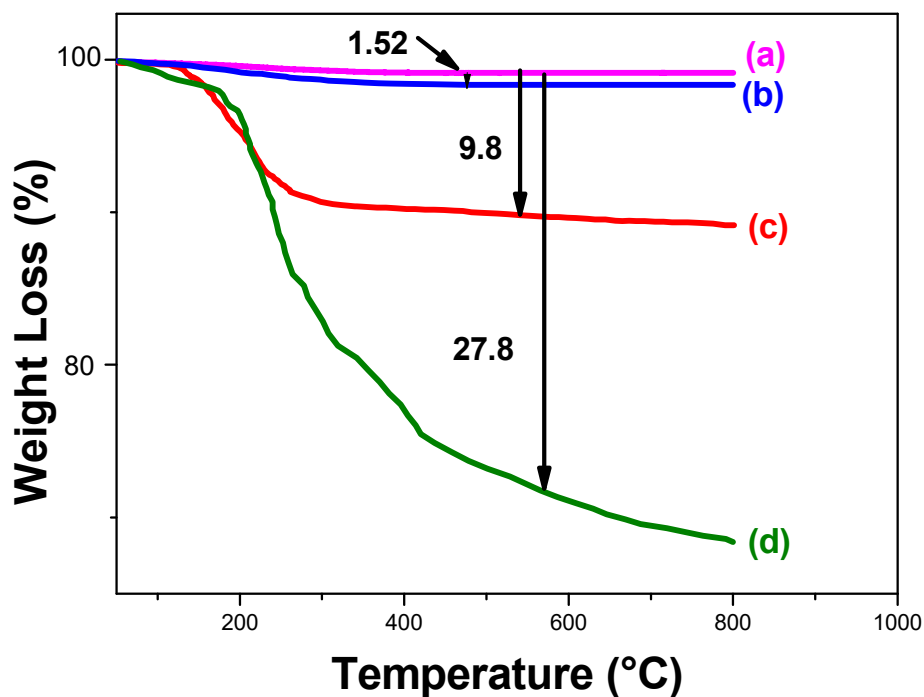

Figure 8. Thermogravimetric analysis (TGA) curves of pristine RuO$_2$-TiO$_2$ NPs (**a**), RuO$_2$-TiO$_2$/PANI (**b**), RuO$_2$-TiO$_2$/DPA (**c**), RuO$_2$-TiO$_2$/DPA/PANI (**d**).

2.3.7. SEM-EDX

Figure 9 depicts SEM images and X-ray emission spectra of the different materials. The images of RuO$_2$-TiO$_2$ mixed oxide reveal the presence of spherical and cubic shaped particles. A contrast has been observed on the image which is directly related to the atomic number Z of the elements containing the analyzed sample; a particle with a high Z appears with a clear contrast; so the bright light spots are attributed to the ruthenium oxide because it is the heaviest element in the heterostructure RuO$_2$-TiO$_2$ NPs (Figure 9a,b). EDS spectrum shows peaks corresponding to Ti and Ru metals as well as a signal attributed to the oxygen molecule, confirming the composition of the simple analyzed and the formation RuO$_2$ and TiO$_2$ oxides (Figure 9c). The SEM images of RuO$_2$-TiO$_2$/PANI show that the particles are aggregated and the morphology is similar to that of pristine RuO$_2$-TiO$_2$ (Figure 9d,e). The corresponding EDS spectrum shows no signal associated to the PANI, which is due to the negligible amount of PANI on the surface of RuO$_2$-TiO$_2$ (Figure 9f). In the presence of DPA, the nanoparticles are much more scattered. The decrease in the agglomeration is very clear (Figure 9g,e). The presence of DPA is testified by the increase in the percentage of carbon on the EDS spectrum. It is noted that is difficult to see the peak of nitrogen when we have a considerable amount of Ti, the latter causes a total masking of the nitrogen signal (Figure 9i). The nanocomposite RuO$_2$-TiO$_2$/DPA/PANI reveals a porous texture and spherical and highly agglomerated particles, which is due to the presence of PANI on the surface of diazonium-modified RuO$_2$-TiO$_2$ (Figure 9j,k); this was confirmed by the EDS spectrum which shows an increase of carbon ratio in the nanocomposite and the appearance of nitrogen and sulfur signals with the decrease of the intensity of Ti and the absence of Ru, which confirms the good coverage of RuO$_2$-TiO$_2$/DPA by PANI (Figure 9l).
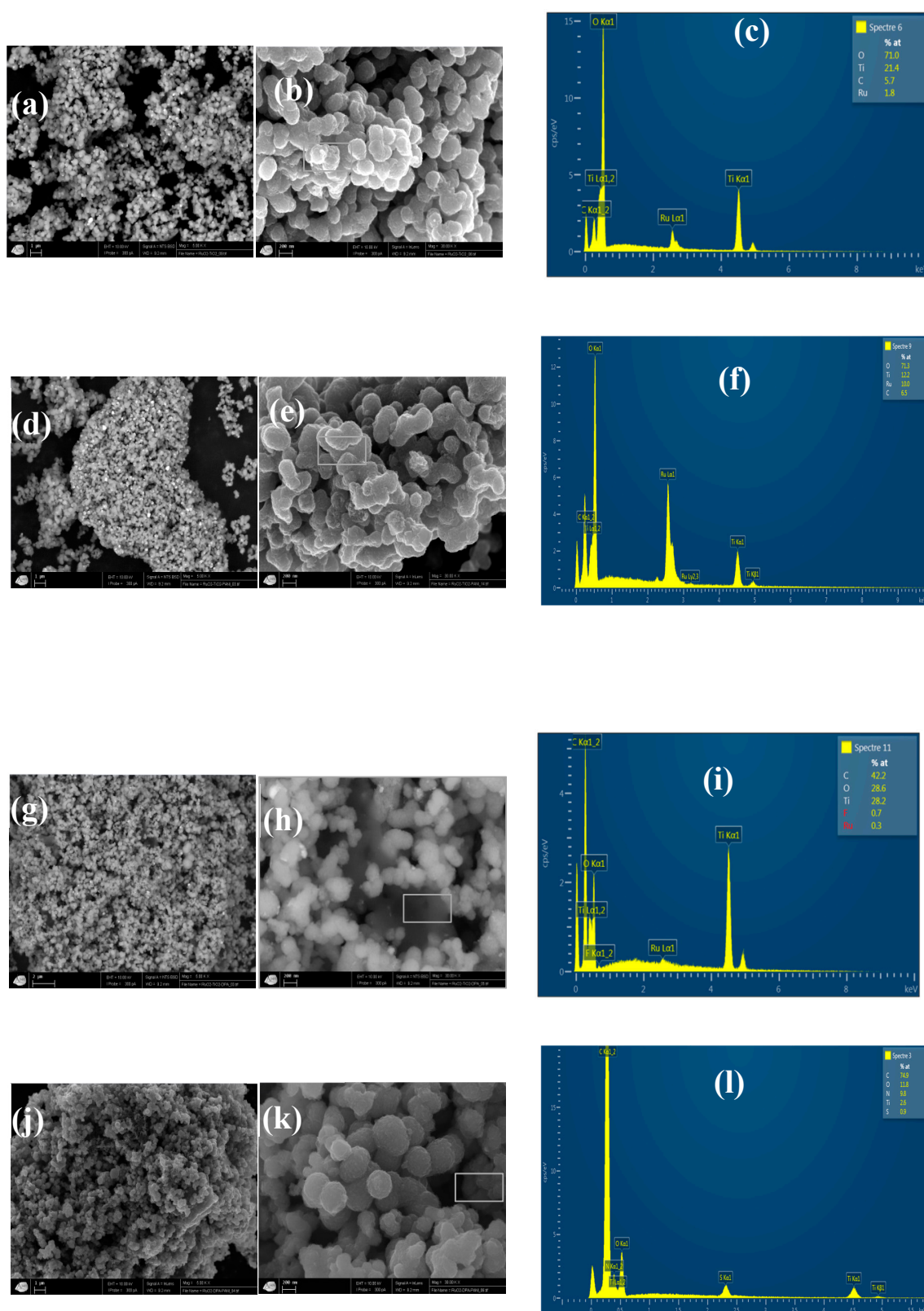
Figure 9. SEM images (**a**,**b**,**d**,**e**,**g**,**h**,**j**,**k**) and elementary spectra (**c**,**f**,**i**,**l**) of RuO_2-TiO_2 NPs (**a**–**c**), RuO_2-TiO_2/PANI (**d**–**f**), RuO_2-TiO_2/DPA (**g**–**i**), RuO_2-TiO_2/DPA/PANI (**j**–**l**).

2.3.8. XPS

The samples were examined by XPS to check the stepwise coating of the underlying photocatalyst by RuO_2-TiO_2 by the DPA aryl layer followed by the PANI top layer.

Figure 10A displays the survey regions of RuO_2-TiO_2 (Figure 10Aa), RuO_2-TiO_2/DPA (Figure 10Ab) and RuO_2-TiO_2/DPA/PANI (Figure 10Ac) which display C1s, N1s, O1s and S2p from PANI as well as the characteristic Ru3d and Ti2p from the photocatalyst (Figure 10Aa-b). The C1s (285 eV) and N1s (400 eV) peaks in Figure 10Ab exhibit higher relative intensity compared to $Ti2p_{3/2}$ (457 eV). No distinct specific peaks from the RuO_2-TiO_2 photocatalysts are noticed in Figure 10Ac which testifies for the efficient screening by PANI due to the DPA adhesive layer. Indeed, sharp C1s, N1s and O1s peaks are noted in Figure 10Ac; they account for PANI. As far as the dopants are concerned, S2p is centered at 169 ev which accounts for sulfates. It is worth noting that for RuO_2-TiO_2/DPA/PANI, S/N atomic ratio = 0.23 which means that the doping level is 46% if we consider the double negative charge of the sulfates. This doping level accounts for the conductivity of PANI. The O/S ratio is ~4.3 indicating that oxygen is essentially due to the SO_4^{2-} dopant.
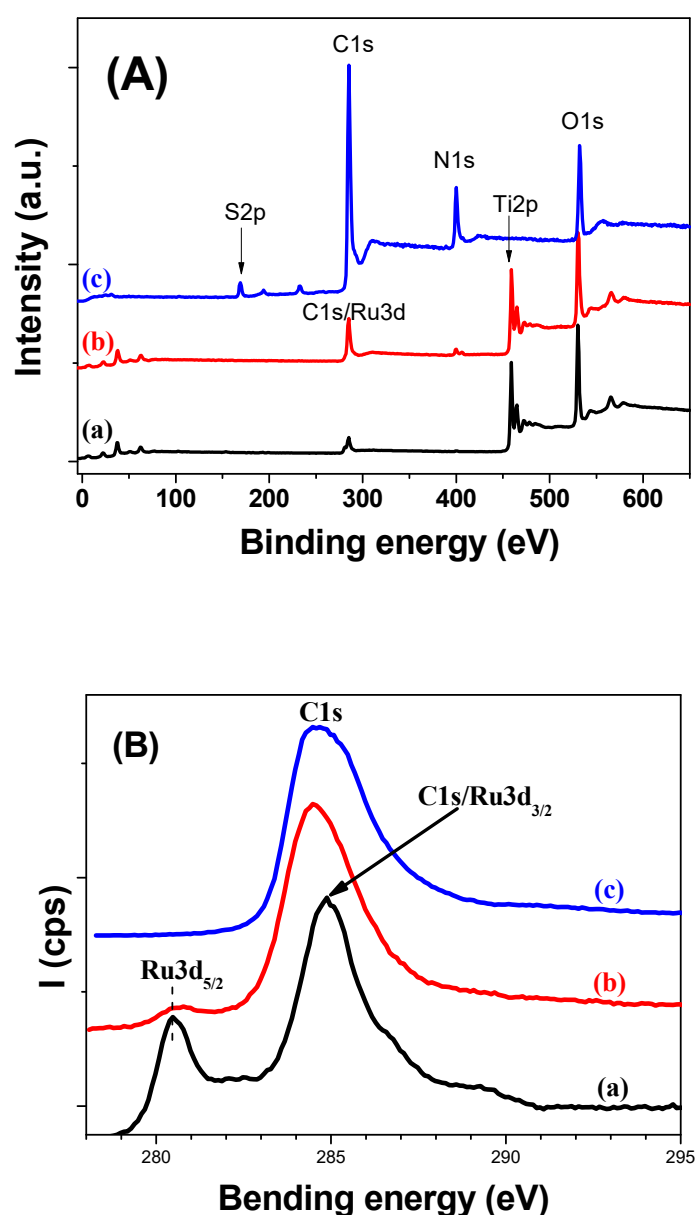

Figure 10. XPS survey scans (**A**) and high resolution C1s spectra (**B**) of RuO_2-TiO_2 (a), RuO_2-TiO_2/DPA (b), and RuO_2-TiO_2/DPA/PANI (c).

Figure 10B displays the high resolution C1s-Ru3d regions; Ru3d$_{5/2}$ is centered at 280.5 eV and Ru3d$_{3/2}$ is lumped with the main C1s component at ~285 eV. The Ru3d$_{5/2}$ is significantly attenuated by the DPA aryl layer meaning that the aryl layer is homogeneous. After in situ polymerization of aniline, the C1s-Ru3d region reduces to the C1s spectrum of pure PANI [73].

2.4. Adhesion of Polyaniline to RuO$_2$-TiO$_2$ Nanoparticles

The diazonium salt acts as a coupling agent, binding the PANI to the surface of RuO$_2$-TiO$_2$ nanoparticles. PANI is soluble in some organic solvents such as N-methyl-2-pyrrolidone (NMP), dimethyl sulfoxide (DMSO), tetrahydrofuran (THF) and hexafluoropropan-2-ol (HFIP) [74,75]. It is thus interesting to investigate the effect of diphenyl amine diazonium (DPA) in the stability of the nanocomposite formed by testing the adhesion of polyaniline to the surface of modified and unmodified nanoparticles in organic polar (DMF, NMP, THF, HFIP and DMSO), and non-polar solvents (chloroform, 1,2-dichloroethane, xylene, toluene). The mixtures of the materials (PANI, RuO$_2$-TiO$_2$/PANI and RuO$_2$-TiO$_2$/DPA/PANI) in organic solvents are shown in Figure 11. The experiment confirmed the solubility of polyaniline in DMSO, NMP, THF and HFIP, while in DMF and toluene the solubility is medium and very low in 1,2-dichloroethane and Xylene (Figure 11A).
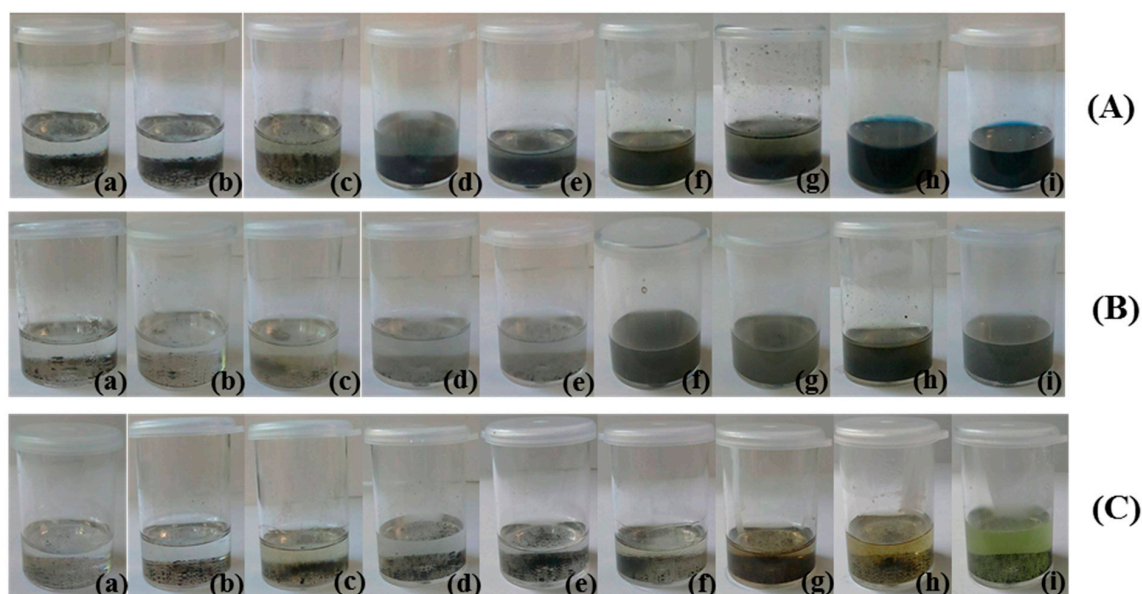

Figure 11. Digital photographs of (**A**): PANI, (**B**): RuO$_2$-TiO$_2$-PANI, (**C**): RuO$_2$-TiO$_2$-DPA-PANI in: (a) Chloroform, (b)1,2-dichloroethane, (c) Xylene, (d)Toluene, (e) DMF, (f) THF, (g) HFIP, (h) NMP, (i) DMSO.

PANI is not adherent on the surface of unmodified RuO$_2$-TiO$_2$ nanoparticles, the solutions turn to a deep green color because of the leaching of PANI from the surface (Figure 11B). The presence of DPA has improved the stability of the nanocomposite by preventing the solubility of PANI in organic solvents. Indeed, the polymer is insoluble thanks to the role of DPA in strengthening the links between PANI and RuO$_2$-TiO$_2$ NPs. It is important to note that when DPA is used, the solutions are all transparent with the exception of a slight staining of DMSO and NMP solutions, due to the dissolution of polymer chains non-related to RuO$_2$-TiO$_2$ surface (Figure 11C). These results are in agreement with those obtained in the case of TiO$_2$ NPs [41] which again confirm the interest of the incorporation of the aryl layer in the nanocomposite.

2.5. Catalytic Performances of RuO$_2$-TiO$_2$-DPA-PANI

Methyl Orange (MO) dye was taken as a model of organic pollutant in order to evaluate the catalytic and photocatalytic abilities of the materials under test. The experiments were carried out with suspensions of 10 mg of catalysts in 50 mL of aqueous methyl orange solution, at a pH of 5.5.

It has been shown that the catalytic activity of materials decreases with increasing pH [76,77]. In acidic medium (pH < 2), MO degradation leads to the formation of quinone as a final product, the latter being much more toxic than the starting molecule [78]. Ammeri et al. [77] demonstrated that the photo-degradation of Methyl Orange is favored at pH < pH$_{PZC}$ of the catalyst, because of the strong adsorption of the Methyl Orange on the catalyst surface positively charged, this is due to the electrostatic attraction of the positive charge of the catalyst surface and the negative charge of the dye.

Before illumination was turned on, the suspensions were stirred magnetically in the dark for 55 minutes (t$_1$) to reach the adsorption equilibrium. However, it was found that the discoloration of MO started during this time under the catalytic effect of the materials, the solutions containing RuO$_2$-TiO$_2$/PANI nanocomposite turned yellow and very light yellow in the presence of RuO$_2$-TiO$_2$/PANI and RuO$_2$-TiO$_2$/DPA/PANI respectively (Figure 12Ac,d), while unmodified RuO$_2$-TiO$_2$ and the solution without any catalyst remained unchanged (Figure 12Aa,b). The suspensions were kept in the dark for more time. The solution of MO containing RuO$_2$-TiO$_2$/DPA/PANI nanocomposite became completely colorless after 75 min (t$_2$ = adsorption time + 20 min) (Figure 12Bd), while that containing the RuO$_2$-TiO$_2$/PANI nanocomposite took about 95 min (t$_3$ = adsorption time + 40 min) (Figure 12Cc); this indicates the role of the catalysts in the activation of the MO degradation process in darkness. The solution containing RuO$_2$-TiO$_2$ nanoparticles and the one containing no catalyst (Figure 12, t$_2$ and t$_3$: a, b) did not undergo any color change. This means that no degradation has taken place and that the catalyst has no catalytic effect at least in the dark.

2 mL of H$_2$O$_2$ were added to non-degraded solutions which were stored in the dark period. The solutions were left again in the dark for 20 min until the organic molecule is absorbed on the surface of RuO$_2$-TiO$_2$ NPs. In order to follow the process of MO photo-degradation in the presence and the absence of the catalyst, samples were taken every 5 min for 15 min and followed by UV-vis analysis. The first sample was taken just before exposing the solution to visible light in order to determine the initial concentration (C$_0$) of the dye. The absorbance of dye solutions before and after irradiation was measured at different degradation time. After 15 min of irradiation, no change in color was recorded in the absence of the catalyst (Figure 13a). However, the presence of RuO$_2$-TiO$_2$ nanoparticles caused total discoloration of the MO (Figure 13b); this highlighted the spectacular role of mixed oxide nanoparticles during the MO degradation process under visible light.
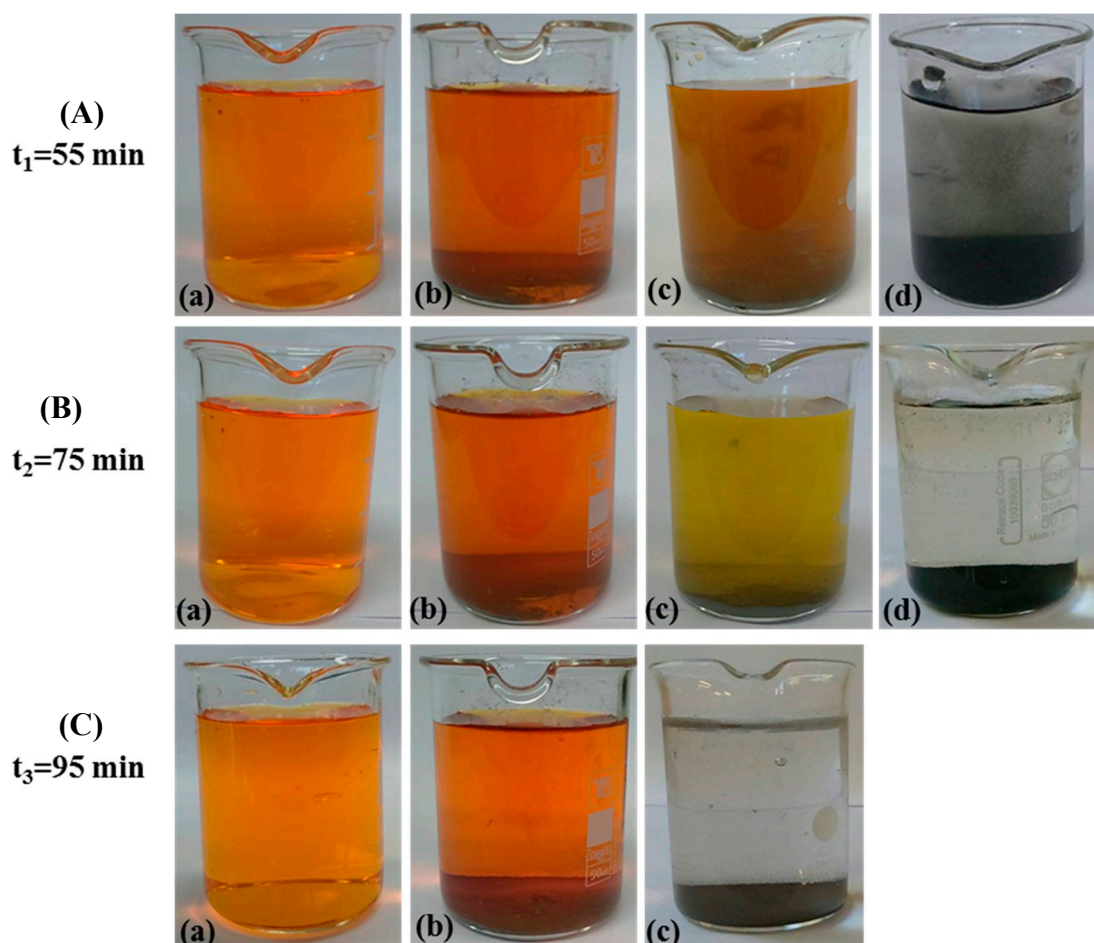
Figure 12. Digital photographs of methyl orange solutions after storage in the dark for (**A**) after t_1 = 55 min, (**B**) after t_2 = 75 min and (**C**) after t_3 = 95 min. (a) Without catalyst, (b) RuO_2-TiO_2 NPs, (c) RuO_2-TiO_2/PANI, (d) RuO_2-TiO_2/DPA/PANI.
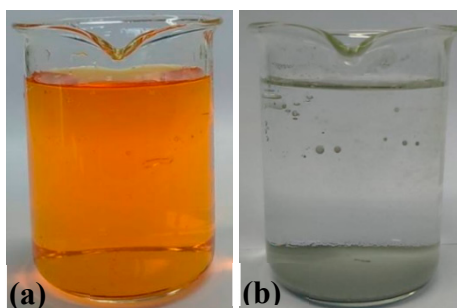

Figure 13. Digital photographs of methyl orange solutions after irradiation for 15 min. (**a**) Without catalyst, (**b**) RuO_2-TiO_2 NPs.

2.5.1. Kinetic Analysis in Darkness

In order to follow the kinetic of MO decomposition in the dark under the catalytic effect of RuO_2-TiO_2/PANI and RuO_2-TiO_2/DPA/PANI nanocomposites, samples were carried out progressively at t_0 = before adsorption, t_1 = adsorption equilibrium (55 min), t_2 = 75 min and t_3 = 95 min, and analyzed with UV-Vis, using a quartz cell and the absorbance measurements were recorded in the range of 200–800 nm.

The UV-vis absorption spectra obtained for the two colorless solutions show the disappearance of the two characteristic bands of methyl orange located between 250–300 nm and 400–500 nm attributed to the phenyl and azo group respectively. This confirms the total decomposition as well as the mineralization of the methyl orange dye solution under the effect of the nanocatalysts (Figure 14c–d). It is noted that the catalytic effect of RuO_2-TiO_2/DPA/PANI is much greater than that of RuO_2-TiO_2/PANI; this is probably due to the amount of PANI loaded in the nanocomposite.
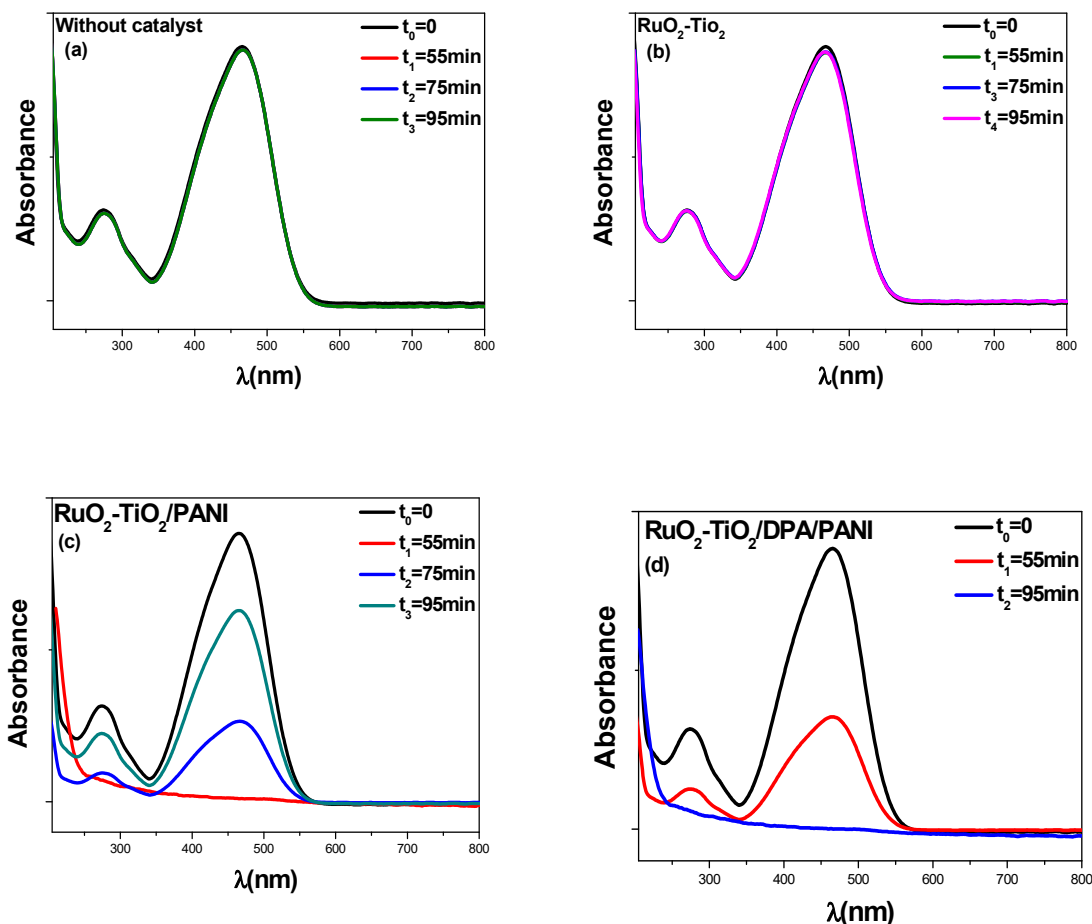

Figure 14. UV-vis absorption spectra of MO solutions before and after storage in darkness. (**a**) Without catalyst, (**b**) RuO_2-TiO_2 NPs, (**c**) RuO_2-TiO_2/PANI, (**d**) RuO_2-TiO_2/DPA/PANI.

The kinetics of MO degradation in the dark in the presence of the RuO_2-TiO_2/PANI and RuO_2-TiO_2/DPA/PANI nanocomposites as a function of the initial concentration of the dye has been reported in Figure 15. The C/C_0 vs. t (min) curves show a negligible degradation rate in the presence of RuO_2-TiO_2 nanoparticles and thus in the absence of catalyst. The dye is completely decomposed under the catalytic effect of the RuO_2-TiO_2/PANI and RuO_2-TiO_2/DPA/PANI nanocomposites, the time required for the removal of the MO varies according to the amount of PANI inserted on the surface of RuO_2-TiO_2 nanoparticles; the degradation rate in the presence of RuO_2-TiO_2/DPA/PANI is much greater than that in the presence of RuO_2-TiO_2/PANI.

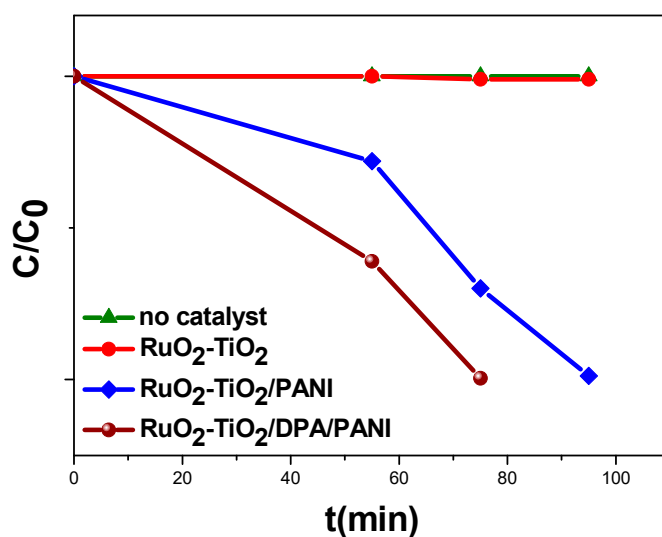**Figure 15.** Kinetics of degradation of Methyl Orange solution ($C = 50mg.L^{-1}$) in the dark.

Many studies have shown that Methyl Orange degradation follow a first-order kinetic [79,80]:

$$Ln \frac{C}{C_0} = -kt$$

where, C_0 is the initial concentration, k (min^{-1}) is the apparent rate constant and C is the concentration of MO. The Ln C/C_0 vs. t(min) plots are linear with correlation coefficients (R) of 0.8573 for RuO_2-TiO_2/PANI and 0.9599 for RuO_2-TiO_2/DAP/PANI nanocatalyst, this shows that the degradation of the MO follows effectively the pseudo-first-order kinetics (Figure 16). The apparent rate constant (min^{-1}) (k_{app}) determined from these plots are 0.0137 and 0.105 min^{-1} in the presence of RuO_2-TiO_2/PANI and RuO_2-TiO_2/DPA/PANI, respectively. These results account for the conductivity measurements made by Four Point Probe (see Section 2.3.1).
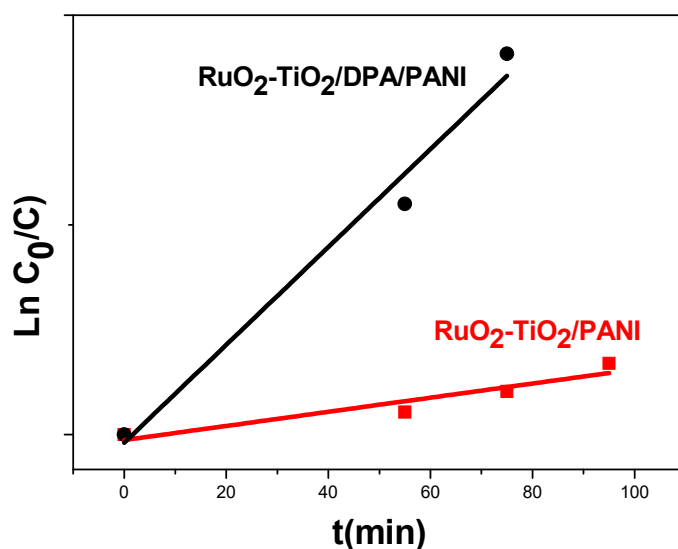

Figure 16. First order linear transforms of the degradation of methyl orange in the dark in the presence of RuO_2-TiO_2/PANI and RuO_2-TiO_2/DPA/PANI nanocomposites.

Catalysis in the dark is an alternative method to photocatalysis, which generally requires a high amount of energy and cannot take place in the absence of light. The oxidative decomposition of organic molecules, in the so-called Fenton reaction, has attracted a lot of attention in recent years, because

it is exempt from the need for light and only requires the presence of a source of the active radicals (OH·, O· and O$^{2-·}$) during the degradation reaction [81]. In this context, several studies have already been undertaken on the catalytic degradation process of organic molecules in the dark, at ambient conditions, without any irradiation and in the presence of metal catalysts [82–84]. Perovskite metal oxides are the most used materials as catalysts in this type of reaction. Liew et al. [85] have studied the catalytic power of perovskite SrFeO$_{3-\delta}$ metal oxide during the decomposition reaction of Bisphenol A and Acid Orange 8. The degradation occurred after 30 h and 60 min respectively in the presence of any reactants generating the formation of radicals. The authors attributed this catalytic effect to the strong adsorption of the organic molecules used on the surface of the catalyst. The same perovskite containing Ba instead of Sr, was used by Sun et al. [86] in the degradation of Acid Orange 8 and the degradation time was five days. This reveals that the cation used in the perovskite compound plays a major role in the catalytic decomposition of pollutants. Using the same material, the degradation of Methyl Orange (20 mg. L^{-1}) in the dark took 50 h [87]. Very recently, Chen and co-workers demonstrated that CuO based metal oxides were very efficient in the degradation of Orange II dye under dark conditions as CaSrCuO$_3$ [81]. Wei et al. [87] prepared the nanocomposite Fe$_3$O$_4$@SiO$_2$@TiO$_2$@MIP in the presence of Methyl Orange and used as the catalyst for the degradation of Congo Red in the darkness at room temperature and atmospheric pressure. The authors found a high catalytic activity of this composite which is due to the polymer which brings to the composite a higher binding capacity toward MO in the binding test compared with the ones that do not contain polymer.
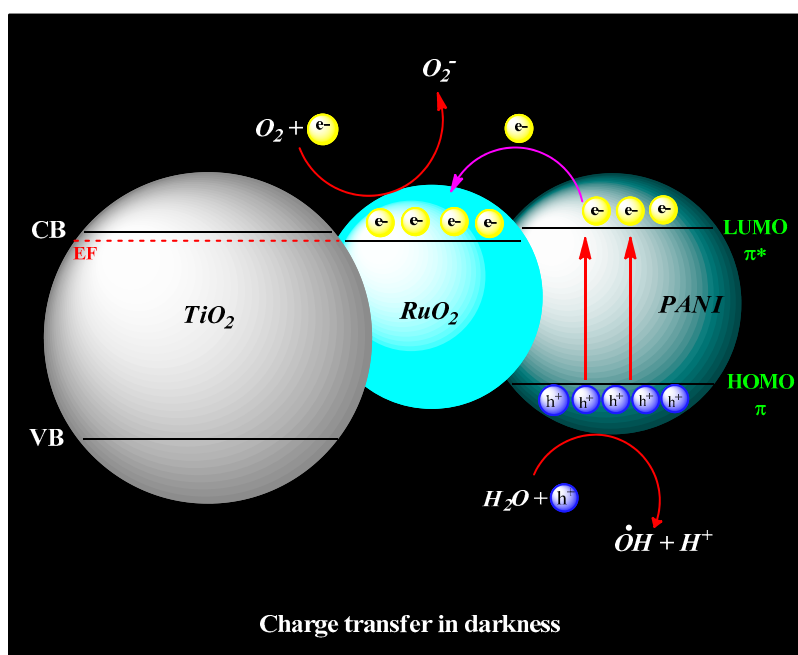
Despite the important catalytic activity that these materials represent in the processes of degradation of organic pollutants, the complete decomposition time remains important compared to our results.

On the one hand, according to Sun et al. [86], the presence of oxygen vacancy in the catalyst structure favors the degradation of MO in the dark. The dye decomposes by oxidation at the oxygen vacancy location of the surface of catalyst. On the other hand, Nguyen et al. [1] associated the catalytic efficiency of the Pt-WO$_3$/Ti-Au nanocomposite to the interfacial contact between WO$_3$ and TiO$_2$ and the Au-induced surface plasmon resonance and the presence of oxygen vacancy in WO$_3$.

TiO$_2$ is a photocatalyst that activates only under UV light; it does not contribute to the degradation process of MO in the dark.

PANI is known as an electron donor; in the dark, the electrons that are stored on the LUMO are released and recovered by RuO$_2$ leaving holes on the HOMO. The electrons and holes are very important in any catalytic process; they promote the formation of OH$^{\bullet}$ radicals and O$_2^{\bullet-}$ anion radicals [1] which are responsible for the decomposition reaction of organic pollutants. To further evidence that holes and superoxide radicals are responsible for degradation in the darkness, it would be interesting to conduct the catalyzed degradation test in darkness using radical scavengers [88,89].

Scheme 1 illustrates the possible mechanism proposed to explain the catalytic activity of RuO$_2$-TiO$_2$/PANI and RuO$_2$-TiO$_2$/DPA/PANI nanocomposites with respect to the degradation reaction of MO dye in the dark.

Scheme 1. Charge transfer in RuO_2-TiO_2/DPA/PANI nanocomposite in darkness.

2.5.2. Kinetic Analysis under Visible Light

UV-vis spectra show a decrease in the intensity of the absorption bands of the MO with the degradation time, after 15 min, the bands disappear completely which is due to the degradation and the mineralization of MO under the catalytic effect of RuO_2-TiO_2 nanoparticles (Figure 17b); this is testified by the C/C_0 plots as a function of the degradation time (Figure 18). The apparent rate constant (k_{app}) found from the curve Ln C_0/C vs. t(min) is 0.106 min^{-1} (Figure 19).

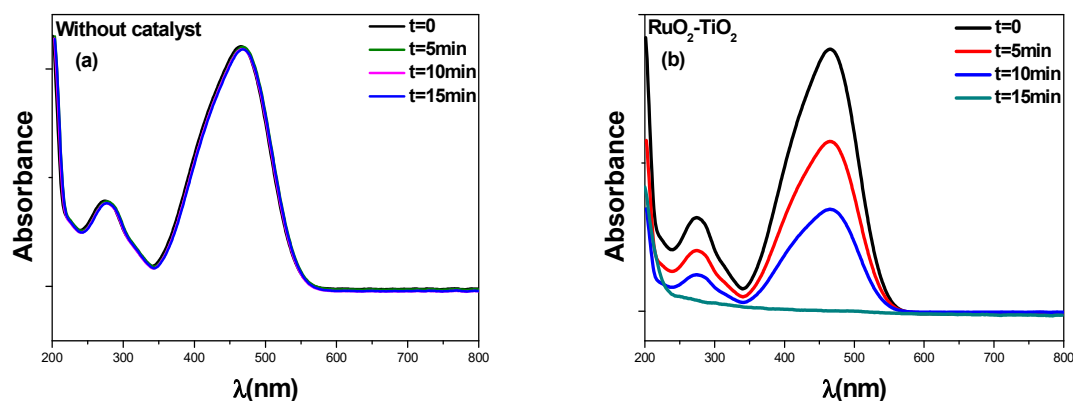**Figure 17.** UV-vis absorption spectra of MO solutions before and after irradiation for various periods. (**a**) without catalyst, (**b**) RuO_2-TiO_2 NPs.
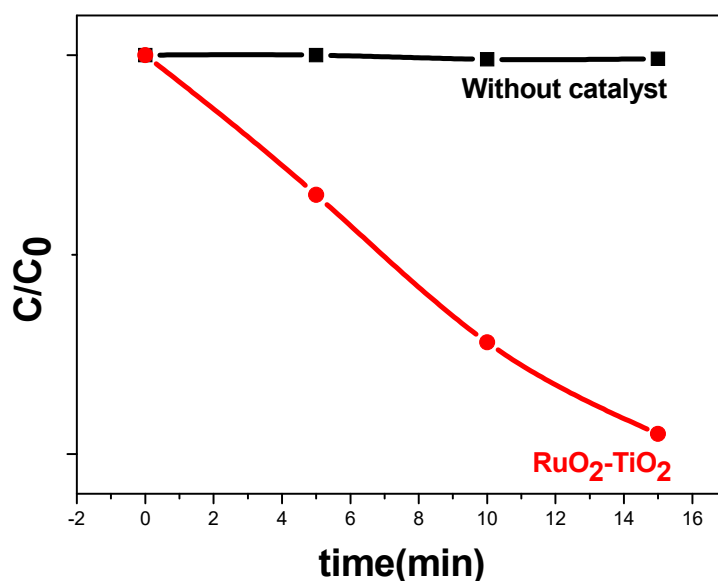
Figure 18. Kinetics of photodegradation of Methyl Orange solution without and in the presence of RuO$_2$-TiO$_2$ catalyst under visible light.
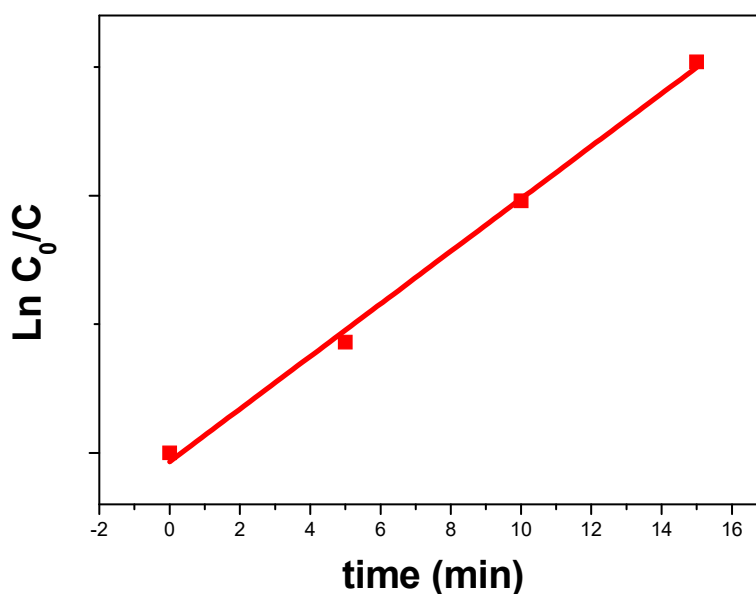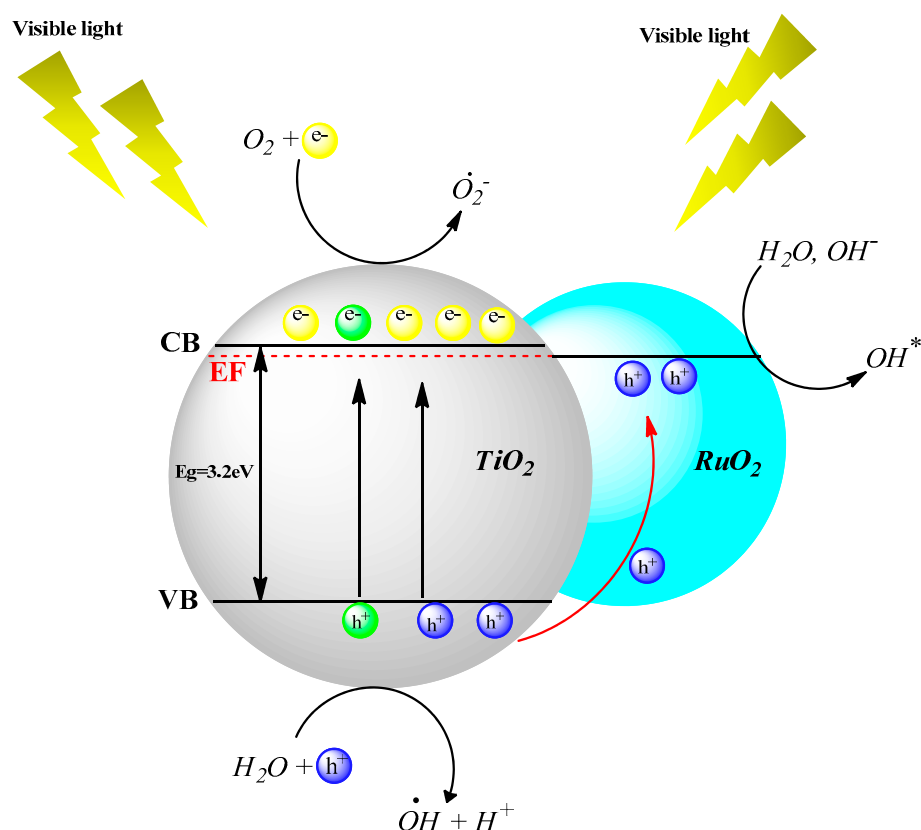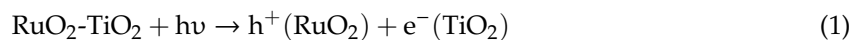

Figure 19. First order linear transforms of the degradation of methyl orange under visible light in the presence of RuO$_2$-TiO$_2$ NPs (R = 0.9955).

The photocatalytic activity of RuO$_2$-TiO$_2$ mixed oxide under sunlight has already been confirmed by other researchers [23,31,90], the RuO$_2$-TiO$_2$ heterostructure exhibits better catalytic performances than that of pure TiO$_2$ and RuO$_2$ [7,23,90]. This is due to the improved separation of the electron-hole pairs and the acceleration of the charge transport at the interface RuO$_2$//TiO$_2$ [7,23].

RuO$_2$ and TiO$_2$ have the same Fermi level; this leads to the formation of electron depletion region at Schottky barrier. Under visible light, the electrons of the TiO$_2$ valence band (VB) are excited and move towards the conduction band (CB), leaving holes in VB. The electron depletion region formed at the Schottky barrier leads to an internal electric field at the TiO$_2$//RuO$_2$ interface. This field is responsible for the separation of the photogenerated electron-hole pairs. The holes and the electrons photogenerated are the most important species in the photocatalytic systems. The electrons on the CB of TiO$_2$ participate in the formation of the O$_2^{\bullet-}$ anion radicals and the holes are responsible for the formation of the OH$^\bullet$ radicals from water and hydrogen peroxide. In addition, the photogenerated

holes which are transferred to RuO_2 leads to the oxidation of H_2O molecules physisorbed on the surface of the nanoparticles, forming oxidizing hydroxyl species which are strongly active in the photocatalytic degradation processes. The mechanism of electron-hole pair separation and the formation of the active species under visible light are described by Scheme 2 and the Equations (1)–(6).

$$RuO_2\text{-}TiO_2 + h\upsilon \rightarrow h^+(RuO_2) + e^-(TiO_2) \tag{1}$$

$$H_2O_2 + h^+ \rightarrow 2\overset{\bullet}{O}H \tag{2}$$

$$H_2O + h^+ \rightarrow \overset{\bullet}{O}H + H^+ \tag{3}$$

$$O_2 \rightarrow O_2{}^* \tag{4}$$

$$O_2{}^* + 1e^- \rightarrow O_2^{\bullet-} \tag{5}$$

$$O^{\ominus}O^{\bullet} \rightarrow H\text{–}O\text{–}O^{\bullet} \tag{6}$$

Scheme 2. Charge transfer in RuO_2-TiO_2 nanoparticles under visible light.

2.5.3. Degradation Extent (%) of Methyl Orange

The percentage of the degradation of the dye was calculated for various degradation times from the following equation [80]:

$$\% = \frac{C_0 - C}{C_0} * 100 \tag{7}$$

where C_0 is the initial concentration of dye and C is the concentration of MO at time t.

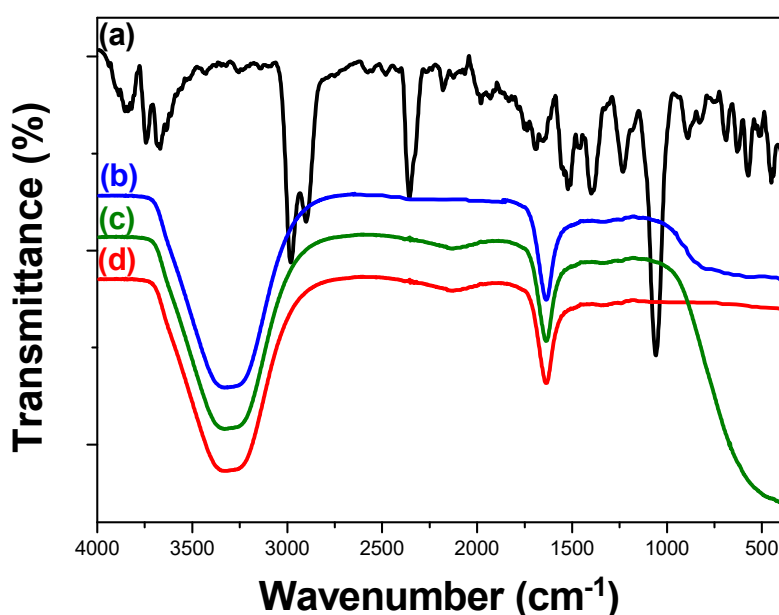The results are summarized in Table 2.

Table 2. Degradation extent (%) of Methyl Orange without and with different catalysts under visible light and darkness.

	Time (min)						
	Darkness				**Visible light**		
Catalysts	**0**	**55**	**75**	**95**	**5**	**10**	**15**
without	0	0	0	0	0	0	0
RuO_2-TiO_2	0	0	0	0.1	36	62	98
RuO_2-TiO_2/PANI	0	57	74	98.7	–	–	–
RuO_2-TiO_2/DPA/PANI	0	67	99.4		–	–	–	–

The photocatalytic effect of RuO_2-TiO_2 under visible light is known, the degradation extent of Methyl Orange increases with the time of the photocatalytic reaction until total decomposition of the dye. The presence of the polyaniline brings benefits not only to the degradation rate and extent of Methyl Orange, but also allows a gain of energy, the addition of PANI to the nanoparticles of RuO_2-TiO_2 mixed oxide makes it a first-class catalyst operating without any irradiation. The degradation percentage of Methyl Orange is higher with RuO_2-TiO_2/DPA/PANI compared to that obtained with RuO_2-TiO_2/PANI nanoparticles in darkness; this depends on the electron exchange between TiO_2 and RuO_2 on the one hand and between RuO_2-TiO_2 and PANI which is known as an electron donor, on the other hand. This again highlights the spectacular role of the diazonium salt as a coupling agent for attaching the PANI to RuO_2-TiO_2 nanoparticles surface.

2.5.4. Degradation Products: Mineralization

MO solution before and after the degradation process was analyzed by infrared spectroscopy in order to identify and to determine the nature of the final products formed with and without irradiation, under the catalytic effect of the various catalysts (RuO_2-TiO_2 under light visible), RuO_2-TiO_2/PANI and RuO_2-TiO_2/DPA/PANI in the dark). Figure 20 illustrates the spectra obtained between 4000 and 400 cm^{-1}.

Figure 20. FTIR spectra of Methyl Orange solutions before (**a**), and after degradation using RuO_2-TiO_2 NPS under visible light (**b**), RuO_2-TiO_2/PANI (**c**) and RuO_2-TiO_2/DPA/PANI (**d**) in the dark.

The spectrum of the initial MO solution (Figure 20a) exhibits a peak around 3429 cm^{-1}, attributed to the N–H stretching vibration. The bands at 2905 and 2854 cm^{-1} are assigned to the C–H stretching vibration of –CH$_3$. The peaks at 1610 and 1540 cm^{-1} are due to the single bond C–C vibration in the aromatic core. At 1426 cm^{-1} is located the N=N vibration band [91,92]. The band centered at 1380 cm^{-1} is corresponding to the vibration –S=O. Two peaks are located at 1225 and 1170 cm^{-1} and are attributed to C–N vibration. The C-H stretching vibrations of the benzene ring are observed at 1030, 847, 816 and 697 cm^{-1} [92]. The bands 624 and 570 cm^{-1} are due to the –C–S stretching vibration [93].

The IR spectra of the degradation products of MO in the presence of RuO$_2$-TiO$_2$ under visible light (Figure 20b), RuO$_2$-TiO$_2$/PANI (Figure 20c) and RuO$_2$-TiO$_2$/DPA/PANI (Figure 20d) in the darkness shows the disappearance of most of the characteristic MO vibration bands, with the appearance of a large and intense peak around 3300 cm^{-1}, corresponding to the vibration of H$_2$O molecules [94]. We also recorded another band at 1637 cm^{-1}, which is due to HCO$_3^-$ from CO$_2$ dissolved in water [95]. These results confirm the decomposition as well as the total mineralization of Methyl Orange and highlight the outstanding catalytic effect of the catalysts used.

2.5.5. Stability of the Catalysts

The long-term use of a catalyst rests on its stability [77]. This property is very important for the evaluation of catalysts and their application [96]. The catalysts already used in the degradation of the MO under and without irradiation were separated, washed several times with the di-ionized water and ethanol and dried at room temperature overnight before reusing them again in the degradation of a new solution of MO. The experiment was carried out under the same conditions as described above (concentration of the solutions, pH, mass of the catalysts, degradation time, hυ, dark).

It was found that all the catalysts present a high stability even after several successive catalytic runs. The results show no decrease in MO degradation rate until the 6th, 8th and 10th test in the presence of RuO$_2$-TiO$_2$, RuO$_2$-TiO$_2$/PANI and RuO$_2$-TiO$_2$/DPA/PANI, respectively, making these catalysts promising for several applications, especially in industry (Figure 21).

Figure 21. Plot of kinetic constants vs. photocatalyzed test number in the presence of RuO$_2$-TiO$_2$, RuO$_2$-TiO$_2$/PANI and RuO$_2$-TiO$_2$/DPA/PANI.
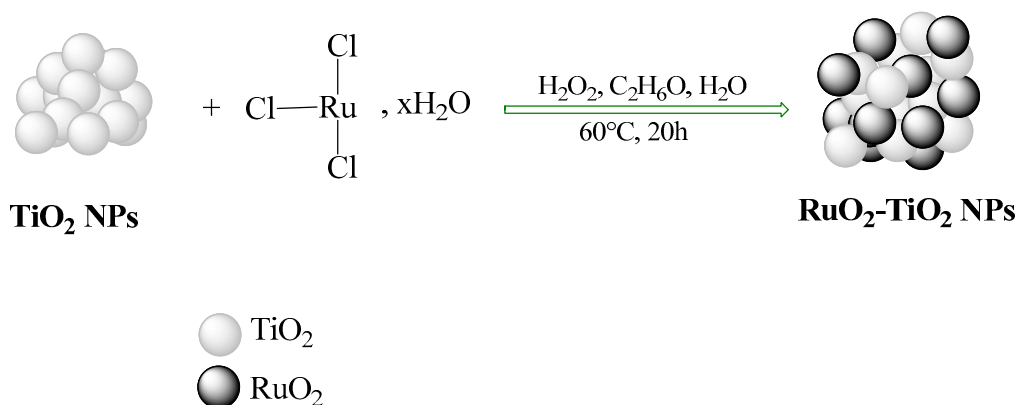
3. Experimental

3.1. Chemicals

The following chemicals were used as received: RuCl$_3$.xH$_2$O (Sigma-Aldrich 98%), TiO$_2$ anatase nanoparticles (prepared by sol-gel [41]), H$_2$O$_2$ (14%), ethanol (99.9%), N-phenyl-p-phenylenediamine

(Alfa Aesar, 98% purity), HBF$_4$ (48%), ascorbic acid, sodium nitrite (Alfa Aesar, Kandel, Germany, purity 99%), ammonium persulfate (APS, Aldrich, Steinheim, Germany, 98% purity), nitric acid (Carlo Erba, 60% purity), aniline (Aldrich, 99.5% pure), Methyl Orange (Sigma-Aldrich, Steinheim, Germany) and the solvents that are Aldrich products: dimethylformamide (DMF), N-methyl-2-pyrrolidone (NMP), tetrahydrofuran (THF), hexafluoropropan-2-ol (HFIP), dimethyl sulfoxide (DMSO), chloroform, 1,2-dichloroethane, xylene and toluene. All aqueous solutions were prepared using deionized water.

3.2. Methods

3.2.1. Preparation of RuO$_2$-TiO$_2$ Powders

RuO$_2$-TiO$_2$ nanoparticles were prepared by sol gel route and reflux process (Scheme 3). 5g (62.6 mmol) of TiO$_2$ nanoparticles prepared in the first stage [41], were dissolved in a mixture of 0.3g (1.34 mmol) of RuCl$_3$·xH$_2$O, 20 mL of hydrogen peroxide (14%) and 10 mL of ethanol. A black colloidal suspension is obtained; this solution is heated under ultrasound operating at a frequency of 50 kHz for two hours at 60 °C in order to disaggregate the particles. After this period of time, 40 mL of distilled water are added drop wise to the solution. The suspension was stirred magnetically and refluxed for 20 h at 60 °C. The resulting gel was dried at 100 °C for 24 h and calcined at 500 °C for 90 min in order to complete the conversion of RuCl$_3$ to RuO$_2$.

Scheme 3. Synthetic route for the preparation of RuO$_2$-TiO$_2$ nanoparticles.

3.2.2. Synthesis of 4-diphenylamine Diazonium Tetrafluoroborate

The synthesis of 4-diphenylamine diazonium tetrafluoroborate carried out according to our previous work [41]. Typically, 0.45 g (2.44 mmol) of N-phenylendiamine was introduced into 5 mL of HBF$_4$ (aqueous solution 48%), stirred at 0 °C for 15 min. Then 0.45g (6.52 mmol of sodium nitrite) was appended to the solution under continuous stirring for 60 min; after that, 60 mL of CH$_2$Cl$_2$ was added to the mixture in order to separate the phases by crystallization. The filtered precipitate is rinsed with ice-cold ether and then dried and kept at a low temperature.

3.2.3. Preparation of RuO$_2$-TiO$_2$/PANI, RuO$_2$-TiO$_2$/DPA/PANI Nanocomposites

The functionalization of RuO$_2$-TiO$_2$ mixed oxide nanoparticles as well as the polymerization of PANI on the surface of RuO$_2$-TiO$_2$ NPs and RuO$_2$-TiO$_2$/DPA were carried out according to the conditions reported in ref. [41].

We reported three chemical methods of grafting of 4-diphenylamine diazonium tetrafluoroborate on the surface of TiO$_2$ nanoparticles. These methods are based on the functionalization of the nanoparticles by in situ generation of aryl diazonium salt, grafting of isolated aryl diazonium and the grafting of isolated diazonium salt in basic medium (diazoate). However, grafting with isolated diazonium salts appears to be the most effective method for modifying TiO$_2$ nanoparticles. Therefore,

it was chosen to modify the nanoparticles of RuO_2-TiO_2 mixed oxide according to the same protocol adopted for the modification of TiO_2 nanoparticles.

The strategy used for the preparation of the RuO_2-TiO_2/DPA/PANI nanocomposite is based on two different protocols. The first pathway consists in grafting of the isolated aryl diazonium molecule previously obtained on the RuO_2-TiO_2 mixed oxide surface: 30 mg of RuO_2-TiO_2 NPs (0.14 mmol) was dispersed in 2 mL of water and sonicated for 20 minutes, then an aqueous solution of diazonium salt (0.28g, 1.04 mmol in 5 mL of H_2O) was poured drop wise with stirring at 0 °C for 15 min, after which, the reducing agent (ascorbic acid 0.4g, 2.27 mmol in 3 mL of H_2O) was added drop wise. The reaction mixture was further stirred for 90 min. The modified nanoparticles were centrifugally separated and washed several times with ethanol then with water, and then dried at room temperature overnight. The second is based on the chemical polymerization of the aniline monomer on the surface of RuO_2-TiO_2 nanoparticles already functionalized with 4-diphenylamine tetrafluoroborate diazonium salt. 0.3 g, (3.23 mmol) of aniline monomer was mixed with nitric acid (0.1g, 1.51 mmol) and stirred for 60 min to form the anilinium cation; to this solution, there was added a suspension of RuO_2-TiO_2/DPA (30 mg, 0.062 mmol) dispersed in 20 mL of acetonitrile ultrasontricated for 10 min, cooled and stirred in ice bath for 120 min. After this time, the initiator (0.4g, 1.75 mmol APS in 5 mL of H_2O) was added drop wise to the above mixture. The reaction was followed by vigorous stirring for 3 h. The resulting precipitate was collected with centrifugation and washed several times with methanol and deionized water to remove any un-reacted species then dried at room temperature for 24 h. The in situ oxidative polymerization of aniline on the surface of RuO_2-TiO_2 was performed following the same approach using the non-functionalized RuO_2-TiO_2 mixed oxide nanoparticles.

3.2.4. Catalytic and Photocatalytic Activity

The catalytic and photocatalytic activity of the various elaborated nanocatalysts were examined by the decomposition of Methyl Orange (MO) in the dark and under visible light. In a typical experiment, to prepared aqueous solutions of Methyl Orange (50 mg/L) catalysts (RuO_2-TiO_2 or RuO_2-TiO_2/PANI or RuO_2-TiO_2/DPA/PANI) were added (10 mg in 50 mL of MO solution, pH = 5.5). The degradation of Methyl Orange was also carried out without catalyst under irradiation in order to observe the effect of visible light on the degradation of the MO. A first sample was taken at the end of the absorption period, without light and just before the light was turned on, and then analyzed by UV-Vis to determine the non-adsorbed dye concentration in solution. Visible light was provided by UVA CUBE 400 (Honle UV technology) and the tests were carried out at room temperature. The mercury lamp emits broad spectrum light covering UV and visible range, the mean radiation is at 365 nm. The mercury lamp power is 500 W.

3.3. Characterization and Instrumentation

The different phases constituting the RuO_2-TiO_2 NPs, RuO_2-TiO_2/DPA and RuO_2-TiO_2/PANI nanocomposites prepared have been identified using a diffractometer (BRUKER AXS D8 ADVANCE, CuKα radiation λ = 1.5418 A°). Surface morphology, distribution of particles and the composition of the samples were checked with a Merlin Carl Zeiss apparatus fitted with energy dispersive X-ray (EDS) analyzer. UV-vis absorbance spectra of the catalysts and MO solution after degradation were measured at room temperature in the wavelength range of 200–800 nm using EVOLUTION 220 UV-Visible spectrometer.

Raman was recorded with Horiba Lab RAM HR Evolution operating at 638 nm at room temperature. Infrared transmittance spectra were assigned using a BRUKER spectrometer operating in ATR mode ranging from 4000 to 400 cm^{-1}.

Thermogravimetric analysis (TGA) was performed on a Setaram instrument Setsys Evolution 16 thermobalance by heating the samples at a rate of 10 °C·min^{-1} from 10 to 800 °C under a flow of air at 20 mL·min^{-1}. X-ray photoelectron spectroscopy analysis (XPS) was performed using K Alpha system (Thermo Fisher Scientific, monochromated Al X-ray source hυ = 1486.6 eV; spot size = 400 μm).

A flood was used for charge compensation and the composition was determined using manufacturer's sensitivity factors.

Other analyzes were performed for RuO_2-TiO_2 mixed oxide only:

The zeta potential measurement was performed to predict the emulsion stability using a zetasizer nano (Malvern Man0485-1.1) that measures the electrophoretic migrations. The measurement was carried out with a suspension consisting of RuO_2-TiO_2 (1 g/l) introduced in 10^{-2} NaCl solution and conducted at different pH of solution adjusted with NaOH and HCl for alkaline and acidic medium respectively. Each measurement is made three times and the size distribution is the average of the three measurements for the consecrated sample.

In order to determine the resistivity of the heterostructure RuO_2-TiO_2 at room temperature, Four Point Resistivity measurement was carried out using KEITHLEY 2601 B source mater by imposing a current of 0.1 mA. The dielectric properties of RuO_2-TiO_2 mixed oxide are also studied by electrical impedance spectroscopy using an impedancemeter HP 4284A. A pellet of RuO_2-TiO_2 is metalized by a very thin layer of silver paste on both sides to ensure contact with the electrodes of the measuring apparatus. The impedance measurements were carried out in the frequency ranging from 100 Hz to 1 MHz and several temperatures under low excitation (1V).

4. Conclusions

A novel catalytic support based on RuO_2-TiO_2 mixed oxide NPs coated PANI was prepared by in situ oxidative polymerization of aniline on diazonium-modified RuO_2-TiO_2 heterostructure. We have demonstrated through this study that this new association combining different materials of type metal-semiconductor n heterostructure and conductive polymer offers spectacular properties to the final materials. The nanocomposites show enhanced catalytic activity in the decomposition of MO in darkness; this activity depends on the presence of PANI on the one hand, and its amount in the final nanocomposite on the other hand, namely. Indeed, the RuO_2-TiO_2 mixed oxide is an excellent photocatalyst under visible light, while the nanocomposite RuO_2-TiO_2/DPA/PANI exhibits significantly improved catalytic performance in the dark compared to RuO_2-TiO_2/PANI nanocomposite. This stresses the role of the diazonium salt as a coupling agent for PANI; it gives the nanocomposite a better thermal and chemical stability, and harnesses adhesion of PANI on the surface of RuO_2-TiO_2 NPs. The enhancement in catalytic activity of designed materials is associated with a synergistic effect between PANI and RuO_2 metal and RuO_2-TiO_2 interfacial contacts which result in the separation of electron-hole pairs and the reduction of its recombination rate. Therefore, RuO_2-TiO_2/DPA/PANI catalyst is highly stable and reusable up to nine times without any loss in catalytic activity, which shows promising potential for practical applications.

In a serendipitous way, while our primary goal was to test the ability of polyaniline to improve the visible light photoactivity of RuO_2-TiO_2 mixed oxide NPs, we have designed in a unique way, unprecedented and highly efficient catalysts for the degradation of pollutants in the darkness. The new catalyst design process is scalable which opens new windows for the general degradation of organic pollutants.

Author Contributions: Conceptualization of the research work: F.M. (Fatima Mousli), A.K., M.M.C.; Methodology: F.M. (Fatima Mousli), A.C., A.K., M.M.C.; Validation: F.M. (Fatima Mousli), A.C., M.J., F.M. (François Maurel), A.K., M.M.C.; Formal Analysis: F.M. (Fatima Mousli), A.C., M.M.C.; Funding acquisition: A.K., M.M.C.; Project administration: M.M.C.; Writing of original draft: F.M. (Fatima Mousli), M.M.C.; Writing—Review & Editing: F.M. (Fatima Mousli), A.C., M.J., F.M. (François Maurel), A.K., M.M.C.; Supervision: A.K., F.M. (François Maurel), M.M.C.

Conflicts of Interest: The authors declare no conflict of interest.

References

1. Nguyen, C.C.; Vu, N.N.; Do, T.O. Efficient hollow double-shell photocatalysts for the degradation of organic pollutants under visible light and in darkness. *J. Mater. Chem A* **2016**, *4*, 4413–4419. [CrossRef]

2. Wu, L.; Bresser, D.; Buchholz, D.; Giffin, G.A.; Castro, C.R.; Ochel, A.; Passerini, S. Unfolding the mechanism of sodium insertion in anatase TiO_2 nanoparticles. *Adv. Energy Mater.* **2015**, *5*, 2. [CrossRef]

3. Tahir, M.; Amin, N.S. Indium-doped TiO_2 nanoparticles for photocatalytic CO_2 reduction with H_2O vapors to CH_4. *Appl. Catal. B Environ.* **2015**, *162*, 98–109. [CrossRef]

4. Bai, S.; Gao, C.; Low, J.; Xiong, Y. Crystal phase engineering on photocatalytic materials for energy and environmental applications. *Nano. Res.* **2018**, 1–24. [CrossRef]

5. Kang, X.; Liu, S.; Dai, Z.; He, Y.; Song, X.; Tan, Z. Titanium Dioxide: From Engineering to Applications. *Catalysts* **2019**, *9*, 191. [CrossRef]

6. Zhou, W.; Yin, Z.; Du, Y.; Huang, X.; Zeng, Z.; Fan, Z.; Liu, H.; Wang, J.; Zhang, H. Synthesis of few-layer MoS_2 nanosheet-coated TiO_2 nanobelt heterostructures for enhanced photocatalytic activities. *Small* **2013**, *9*, 140–147. [CrossRef]

7. Uddin, M.T.; Nicolas, Y.; Olivier, C.; Toupance, T.ä.; Müller, M.M.; Kleebe, H.J.; Rachut, K.; Ziegler, J.; Klein, A.; Jaegermann, W. Preparation of RuO_2/TiO_2 mesoporous heterostructures and rationalization of their enhanced photocatalytic properties by band alignment investigations. *J. Phys. Chem. C* **2013**, *117*, 22098–22110. [CrossRef]

8. Cao, B.; Li, G.; Li, H. Hollow spherical $RuO_2@TiO_2@Pt$ bifunctional photocatalyst for coupled H_2 production and pollutant degradation. *Appl. Catal. B Environ.* **2016**, *194*, 42–49. [CrossRef]

9. Yang, H.; Bright, J.; Kasani, S.; Zheng, P.; Musho, T.; Chen, B.; Huang, L.; Wu, N. Metal–organic framework coated titanium dioxide nanorod array p–n heterojunction photoanode for solar water-splitting. *Nano. Res.* **2019**, *12*, 643–650. [CrossRef]

10. Chakraborty, A.K.; Hossain, M.E.; Rhaman, M.M.; Sobahan, K.M.A. Fabrication of Bi_2O_3/TiO_2 nanocomposites and their applications to the degradation of pollutants in air and water under visible-light. *J. Environ. Sci.* **2014**, *26*, 458–465. [CrossRef]

11. Kongsong, P.; Sikong, L.; Masae, M.; Singsang, W.; Niyomwas, S.; Rachpech, V. Photocatalytic antibacterial performance of PVP-doped SnO_2/TiO_2 thin films coated on glass fibers. *Songklanakarin J. Sci. Technol.* **2018**, *40*, 659–665. [CrossRef]

12. Zhang, L.; Yu, W.; Han, C.; Guo, J.; Zhang, Q.; Xie, H.; Guo, Z. Large scaled synthesis of heterostructured electrospun TiO_2/SnO_2 nanofibers with an enhanced photocatalytic activity. *J. Electrochem. Soc.* **2017**, *164*, H651–H656. [CrossRef]

13. Rudakova, A.V.; Emeline, A.V.; Bahnemann, D.W. Effect of the TiO_2-ZnO Heterostructure on the Photoinduced Hydrophilic Conversion of TiO_2 and ZnO Surfaces. *J. Phys. Chem. C* **2019**, *123*. [CrossRef]

14. Wang, D.P.; Zeng, H.C. Multifunctional roles of TiO_2 nanoparticles for architecture of complex core− shells and hollow spheres of $SiO_2−TiO_2−$polyaniline system. *Chem. Mater.* **2009**, *21*, 4811–4823. [CrossRef]

15. Eskandari, P.; Farhadian, M.; Solaimany Nazar, A.R.; Jeon, B.H. Adsorption and photodegradation efficiency of $TiO_2/Fe_2O_3/PAC$ and $TiO_2/Fe_2O_3/$zeolite nanophotocatalysts for the removal of cyanide. *Ind. Eng. Chem. Res.* **2019**, *58*, 2099–2112. [CrossRef]

16. Yao, L.; Wang, W.; Wang, L.; Liang, Y.; Fu, J.; Shi, H. Chemical bath deposition synthesis of TiO_2/Cu_2O core/shell nanowire arrays with enhanced photoelectrochemical water splitting for H_2 evolution and photostability. *Inter. J. Hydrogen Energy.* **2018**, *43*, 15907–15917. [CrossRef]

17. Chen, Z.; Gao, Y.; Zhang, Q.; Li, L.; Ma, P.; Xing, B.; Zhang, Z. $TiO_2/NiO/$reduced graphene oxide nanocomposites as anode materials for high-performance lithium ion batteries. *J. Alloys. Compd.* **2019**, *774*, 873–878. [CrossRef]

18. Saavedra, J.; Pursell, C.J.; Chandler, B.D. CO oxidation kinetics over Au/TiO_2 and Au/Al_2O_3 catalysts: evidence for a common water-assisted mechanism. *J. Am. Chem. Soc.* **2018**, *140*, 3712–3723. [CrossRef]

19. Petronella, F.; Truppi, A.; Striccoli, M.; Curri, M.L.; Comparelli, R. Photocatalytic Application of Ag/TiO_2 Hybrid Nanoparticles. In *Noble Metal-Metal Oxide Hybrid Nanoparticles*; Woodhead Publishing: Cambridge, UK, 2019.

20. Wang, F.; Wong, R.J.; Ho, J.H.; Jiang, Y.; Amal, R. Sensitization of Pt/TiO$_2$ using plasmonic Au nanoparticles for hydrogen evolution under visible-light irradiation. *ACS Appl. Mater. Inter.* **2017**, *9*, 30575–30582. [CrossRef]

21. Tian, J.; Zhao, Z.; Kumar, A.; Boughton, R.I.; Liu, H. Recent progress in design, synthesis, and applications of one-dimensional TiO$_2$ nanostructured surface heterostructures: a review. *Chem. Soc. Rev.* **2014**, *43*, 6920–6937. [CrossRef]

22. Panić, V.; Dekanski, A.; Wang, G.; Fedoroff, M.; Milonjić, S.; Nikolić, B. Morphology of RuO$_2$–TiO$_2$ coatings and TEM characterization of oxide sols used for their preparation. *J. Colloid. Inter. Sci.* **2003**, *263*, 68–73. [CrossRef]

23. Tian, J.; Hu, X.; Wei, N.; Zhou, Y.; Xu, X.; Cui, H.; Liu, H. RuO$_2$/TiO$_2$ nanobelt heterostructures with enhanced photocatalytic activity and gas-phase selective oxidation of benzyl alcohol. *Sol. Energy Mater. Sol. Cells.* **2016**, *151*, 7–13. [CrossRef]

24. Näslund, L.Å.; Sánchez-Sánchez, C.M.; Ingason, Á.S.; Bäckström, J.; Herrero, E.; Rosen, J.; Holmin, S. The role of TiO$_2$ doping on RuO$_2$-coated electrodes for the water oxidation reaction. *J. Phys. Chem. C.* **2013**, *117*, 6126–6135. [CrossRef]

25. Mitsuhashi, T.; Watanabe, A. Anomalies in heat capacity measurements of RuO$_2$-TiO$_2$ system. *J. Therm. Anal. Calorim.* **2000**, *60*, 683–689. [CrossRef]

26. Riga, J.; Tenret-Noel, C.; Pireaux, J.J.; Caudano, R.; Verbist, J.J.; Gobillon, Y. Electronic structure of rutile oxides TiO$_2$, RuO$_2$ and IrO$_2$ studied by X-ray photoelectron spectroscopy. *Phys. Scr.* **1977**, *16*, 351. [CrossRef]

27. Ismail, A.A.; Bahnemann, D.W.; Al-Sayari, S.A. Synthesis and photocatalytic properties of nanocrystalline Au, Pd and Pt photodeposited onto mesoporous RuO$_2$-TiO$_2$ nanocomposites. *App. Catal A Gen.* **2012**, *431*, 62–68. [CrossRef]

28. Silva, L.M.; dos Santos, R.P.; Morais, C.C.; Vasconcelos, C.L.; Martínez-Huitle, C.A.; Castro, S.S. Anodic oxidation of the insecticide imidacloprid on mixed metal oxide (RuO$_2$-TiO$_2$ and IrO$_2$-RuO$_2$-TiO$_2$) anodes. *J. Electrochim. Soc.* **2017**, *164*, E489–E495. [CrossRef]

29. Jiao, Y.; Jiang, H.; Chen, F. RuO$_2$/TiO$_2$/Pt ternary photocatalysts with epitaxial heterojunction and their application in CO oxidation. *Acs. Catal.* **2014**, *4*, 2249–2257. [CrossRef]

30. Kuramasu, K.; Saito, S.; Okano, K.; Takahashi, Y. Resistor film by thermal decomposition technique and thermal decomposition characteristics of its source materials. *J. Ceram. Soc. Jpn.* **1996**, *104*, 844–849. [CrossRef]

31. Ismail, A.A.; Robben, L.; Bahnemann, D.W. Study of the Efficiency of UV and Visible-Light Photocatalytic Oxidation of Methanol on Mesoporous RuO$_2$–TiO$_2$ Nanocomposites. *ChemPhysChem* **2011**, *12*, 982–991. [CrossRef]

32. Houšková, V.; Štengl, V.; Bakardjieva, S.; Murafa, N.; Tyrpekl, V. Efficient gas phase photodecomposition of acetone by Ru-doped Titania. *Appl. Catal. B Environ.* **2009**, *89*, 613–619. [CrossRef]

33. Amama, P.B.; Itoh, K.; Murabayashi, M. Effect of RuO$_2$ deposition on the activity of TiO$_2$: Photocatalytic oxidation of trichloroethylene in aqueous phase. *J. mater.Sci.* **2004**, *39*, 4349–4351. [CrossRef]

34. Košević, M.; Stopic, S.; Cvetković, V.; Schroeder, M.; Stevanović, J.; Panić, V.; Friedrich, B. Mixed RuO$_2$/TiO$_2$ uniform microspheres synthesized by low-temperature ultrasonic spray pyrolysis and their advanced electrochemical performances. *Appl. Surf. Sci.* **2019**, *464*, 1–9. [CrossRef]

35. Panić, V.; Dekanski, A.; Milonjić, S.; Atanasoski, R.; Nikolić, B. The influence of the aging time of RuO$_2$ and TiO$_2$ sols on the electrochemical properties and behavior for the chlorine evolution reaction of activated titanium anodes obtained by the sol-gel procedure. *Electrochim. Acta.* **2000**, *46*, 415–421. [CrossRef]

36. Mitrovic, D.; Panic, V.; Dekanski, A.L.E.K.S.A.N.D.A.R.; Milonjic, S.; Atanasoski, R.A.D.O.S.L.A.V.; Nikolic, B. The effect of the composition of the dispersing medium of oxide sols on the electrocatalytic activity of sol-gel obtained RuO$_2$-TiO$_2$/Ti anodes. *J. Serb. Chem. Soc.* **2001**, *66*, 847–858. [CrossRef]

37. Buenviaje, J.S.C.; Usman, K.A.S.; Payawan, J.L.M. *AIP Conference Proceedings*; AIP Publishing: Melville, NY, USA, 2018; Volume 1958, p. 020015.

38. Gnanasekaran, L.; Hemamalini, R.; Naushad, M. Efficient photocatalytic degradation of toxic dyes using nanostructured TiO$_2$/polyaniline nanocomposite. *Water Treat.* **2018**, *108*, 322–328. [CrossRef]

39. Zhao, Z.; Zhou, Y.; Wan, W.; Wang, F.; Zhang, Q.; Lin, Y. Nanoporous TiO$_2$/polyaniline composite films with enhanced photoelectrochemical properties. *Mater. Lett.* **2014**, *130*, 150–153. [CrossRef]

40. Li, J.; Xiao, Q.; Li, L.; Shen, J.; Hu, D. Novel ternary composites: Preparation, performance and application of ZnFe$_2$O$_4$/TiO$_2$/polyaniline. *Appl. Surf. Sci.* **2015**, *331*, 108–114. [CrossRef]

41. Mousli, F.; Chaouchi, A.; Hocine, S.; Lamouri, A.; Vilar, M.R.; Kadri, A.; Chehimi, M.M. Diazonium-modified TiO$_2$/polyaniline core/shell nanoparticles. Structural characterization, interfacial aspects and photocatalytic performances. *App. Surf. Sci.* **2019**, *465*, 1078–1095. [CrossRef]

42. Chehimi, M.M. *Aryl Diazonium Salts: New Coupling Agents in Polymer and Surface Science*; Wiley-VCH: Weinheim, Germany, 2012.

43. Mohamed, A.A.; Salmi, Z.; Dahoumane, S.A.; Mekki, A.; Carbonnier, B.; Chehimi, M.M. Functionalization of nanomaterials with aryldiazonium salts. *Adv. Colloid. Interface Sci.* **2015**, *225*, 16–36. [CrossRef] [PubMed]

44. Mirkhalaf, F.; Graves, J.E. Nanostructured electrocatalysts immobilised on electrode surfaces and organic film templates. *Chem. Pap.* **2012**, *66*, 472–483. [CrossRef]

45. Salmi, Z.; Gam-Derouich, S.; Mahouche-Chergui, S.; Turmine, M.; Chehimi, M. On the interfacial chemistry of aryl diazonium compounds in polymer science. *Chem. Pap.* **2012**, *66*, 369–391. [CrossRef]

46. Lo, M.; Pires, R.; Diaw, K.; Gningue-Sall, D.; Oturan, M.A.; Aaron, J.J.; Chehimi, M.M. Diazonium salts: versatile molecular glues for sticking conductive polymers to flexible electrodes. *Surfaces* **2018**, *1*, 5. [CrossRef]

47. Marques, F.C.; Canela, M.C.; Stumbo, A.M. Hydrogen Production from Aqueous Solutions of Glycerol on TiO$_2$/Ru-MCM-41 Photocatalysts Using Solar Light. *Top. Catal.* **2017**, *60*, 1196–1209. [CrossRef]

48. Li, Y.; Qin, Z.; Guo, H.; Yang, H.; Zhang, G.; Ji, S.; Zeng, T. Low-temperature synthesis of anatase TiO$_2$ nanoparticles with tunable surface charges for enhancing photocatalytic activity. *PLoS ONE* **2014**, *9*, e114638. [CrossRef] [PubMed]

49. Mianxince, S.O.N.G.; Liang, B.; Tianliang, Z.; Xiaoyong, Z.H.A.O. Surface potential and photocatalytic activity of rare earths doped TiO$_2$. *J. Rare Earths.* **2008**, *26*, 693–699.

50. Uchikoshi, T.; Suzuki, T.S.; Iimura, S.; Tang, F.; Sakka, Y. Control of crystalline texture in polycrystalline TiO$_2$ (Anatase) by electrophoretic deposition in a strong magnetic field. *J. Eur. Ceram. Soc.* **2006**, *26*, 559–563. [CrossRef]

51. Gogoi, P.; Kumar, T.S.; Sharma, P.; Pamu, D. Structural, optical, dielectric and electrical studies on RF sputtered nanocrystalline Zr doped MgTiO$_3$ thin films. *J. Alloys Comp.* **2015**, *619*, 527–537. [CrossRef]

52. Tabib, A.; Sdiri, N.; Elhouichet, H.; Férid, M. Investigations on electrical conductivity and dielectric properties of Na doped ZnO synthesized from sol gel method. *J. Alloys Compd.* **2015**, *622*, 687–694. [CrossRef]

53. Badr, A.M.; Elshaikh, H.A.; Ashraf, I.M. Impacts of temperature and frequency on the dielectric properties for insight into the nature of the charge transports in the Tl2S layered single crystals. *J. Mod. Phys.* **2011**, *2*, 12. [CrossRef]

54. Fröhlich, K.; Cambel, V.; Machajdík, D.; Baumann, P.K.; Lindner, J.; Schumacher, M.; Juergensen, H. Low-temperature growth of RuO$_2$ films for conductive electrode applications. *Mater. Sci. Semicond. Proc.* **2002**, *5*, 173–177. [CrossRef]

55. Jelenkovic, E.V.; Tong, K.Y.; Cheung, W.Y.; Wong, S.P. RuO$_2$–SiO$_2$ composite thin films with wide resistivity range. *Microelectron. Eng.* **2004**, *71*, 237–241. [CrossRef]

56. Huang, J.H.; Chen, J.S. Material characteristics and electrical property of reactively sputtered RuO$_2$ thin films. *Thin Solid Films.* **2001**, *382*, 139–145. [CrossRef]

57. Cao, Y.; Smith, P.; Heeger, A.J. Counter-ion induced processibility of conducting polyaniline and of conducting polyblends of polyaniline in bulk polymers. *Synth. Met.* **1992**, *48*, 91. [CrossRef]

58. Hadj Salah, N. Etude de la dégradation photocatalytique de polluants organiques en présence de dioxyde de titane, en suspension aqueuse et en lit fixe. Ph.D. Thesis, Université de Grenoble, Saint-Martin-d'Hères, France, 2012. Available online: https://tel.archives-ouvertes.fr/tel-00781668/ (accessed on 28 March 2019).

59. Gao, L.B.; Liu, S.H.; Zhang, L.Y.; Shi, L.X.; Chen, Z.N. Preparation, Characterization, Redox Properties, and UV−Vis−NIR Spectra of Binuclear Ruthenium Complexes [{(Phtpy)(PPh$_3$)$_2$Ru}$_2${C$\overset{\cdot}{\cdot}$C−(CH=CH)$_m$−C$\overset{\cdot}{\cdot}$C}]$^{n+}$ (Phtpy = 4′-phenyl-2,2′:6,2″-terpyridine). *Organometallics* **2006**, *25*, 506–512. [CrossRef]

60. Uddin, M.T. Metal oxide heterostructures for efficient photocatalysts. Ph.D. Thesis, Université Sciences et Technologies-Bordeaux I, Talence, France, 2013. Available online: https://tel.archives-ouvertes.fr/tel-00879226/ (accessed on 1 April 2019).

61. Li, X.; Wang, D.; Cheng, G.; Luo, Q.; An, J.; Wang, Y. Preparation of polyaniline-modified TiO$_2$ nanoparticles and their photocatalytic activity under visible light illumination. *Appl. Catal B Environ.* **2008**, *81*, 267–273. [CrossRef]

62. Wahyuni, S.; Kunarti, E.S.; Swasono, R.T.; Kartini, I. Characterization and Photocatalytic Activity of TiO$_2$ (rod)-SiO$_2$-Polyaniline Nanocomposite. *Indones. J. Chem.* **2018**, *18*, 321–330.

63. Masid, S.; Tayade, R.; Rao, N.N. Efficient visible light active polyaniline/TiO$_2$ nanocomposite photocatalyst for degradation of Reactive Blue 4. *Int. J. Photocatal. Photon.* **2015**, *119*, 190–203.

64. Min, S.; Wang, F.; Han, Y. An investigation on synthesis and photocatalytic activity of polyaniline sensitized nanocrystalline TiO$_2$ composites. *J. Mater. Sci.* **2007**, *42*, 9966–9972. [CrossRef]

65. Musić, S.; Popović, S.; Maljković, M.; Furić, K.; Gajović, A. Influence of synthesis procedure on the formation of RuO$_2$. *Mater. Lett.* **2002**, *56*, 806–811. [CrossRef]

66. Leroux, Y.R.; Fei, H.; Noël, J.M.; Roux, C.; Hapiot, P. Efficient covalent modification of a carbon surface: use of a silyl protecting group to form an active monolayer. *J. Am. Chem. Soc.* **2010**, *132*, 14039–14041. [CrossRef] [PubMed]

67. Orefuwa, S.A.; Ravanbakhsh, M.; Neal, S.N.; King, J.B.; Mohamed, A.A. Robust Organometallic Gold Nanoparticles. *Organometallics* **2013**, *33*, 439–442. [CrossRef]

68. Tanzifi, M.; Hosseini, S.H.; Kiadehi, A.D.; Olazar, M.; Karimipour, K.; Rezaiemehr, R.; Ali, I. Artificial neural network optimization for methyl orange adsorption onto polyaniline nano-adsorbent: kinetic, isotherm and thermodynamic studies. *J. Mol. Liquids.* **2017**, *244*, 189–200. [CrossRef]

69. Baibarac, M.; Baltog, I.; Frunza, S.; Magrez, A.; Schur, D.; Zaginaichenko, S.Y. Single-walled carbon nanotubes functionalized with polydiphenylamine as active materials for applications in the supercapacitors field. *Diamond. Relat. Mater.* **2013**, *32*, 72–82. [CrossRef]

70. Chen, Y.M.; Korotcov, A.; Hsu, H.P.; Huang, Y.S.; Tsai, D.S. Raman scattering characterization of well-aligned RuO$_2$ nanocrystals grown on sapphire substrates. *New J. Phys.* **2007**, *9*, 130. [CrossRef]

71. Ceballos-Chuc, M.C.; Ramos-Castillo, C.M.; Alvarado-Gil, J.J.; Oskam, G.; Rodríguez-Gattorno, G. Influence of Brookite Impurities on the Raman Spectrum of TiO$_2$ Anatase Nanocrystals. *J. Phys. Chem. C* **2018**, *122*, 19921–19930. [CrossRef]

72. Mar, S.Y.; Chen, C.S.; Huang, Y.S.; Tiong, K.K. Characterization of RuO$_2$ thin films by Raman spectroscopy. *Appl. Surf. Sci.* **1995**, *90*, 497–504. [CrossRef]

73. Barthet, C.; Armes, S.P.; Chehimi, M.M.; Bilem, C.; Omastova, M. Surface characterization of polyaniline-coated polystyrene latexes. *Langmuir.* **1998**, *14*, 5032–5038. [CrossRef]

74. Bıçak, N.; Şenkal, B.F.; Sezer, E. Preparation of organo-soluble polyanilines in ionic liquid. *Synth. Met.* **2005**, *155*, 105–109. [CrossRef]

75. Wang, Y.; Zheng, H.; Jia, L.; Li, H.; Li, T.; Chen, K.; Gu, Y. Optimizing the polymerization conditions of soluble polyaniline doped with itaconic acid. *J. Macromol. Sci. Part A* **2014**, *51*, 577–581. [CrossRef]

76. Wang, Z.; Shen, L.; Zhu, S. Synthesis of Core-Shell Fe$_3$O$_4$@SiO$_2$@TiO$_2$ microspheres and Their Application as Recyclable Photocatalysts. *Int. J. Photoenergy.* **2012**. [CrossRef]

77. Ammuri, A.; Hejiouej, S.; Ziat, K.; Saidi, M. Dégradation photo-catalytique d'un colorant azoïque, orange de méthyle, par une suspension aqueuse de trioxyde de bismuth (photodegradation of methyl orange in solution in presence of bismuth trioxide). *Mater. Environ. Sci.* **2014**, *5*, 2066–2072.

78. Chen, L.C.; Tsai, F.R.; Huang, C.M. Photocatalytic decolorization of methyl orange in aqueous medium of TiO$_2$ and Ag–TiO$_2$ immobilized on γ-Al$_2$O$_3$. *J. Photochem. Photobiol A Chem.* **2005**, *170*, 7–14. [CrossRef]

79. Islam, M.T.; Jing, H.; Yang, T.; Zubia, E.; Goos, A.G.; Bernal, R.A.; Noveron, J.C. Fullerene stabilized gold nanoparticles supported on titanium dioxide for enhanced photocatalytic degradation of methyl orange and catalytic reduction of 4-nitrophenol. *J. Environ. Chem. Eng.* **2018**, *6*, 3827–3836. [CrossRef]

80. Saleh, T.A.; Gupta, V.K. Photo-catalyzed degradation of hazardous dye methyl orange by use of a composite catalyst consisting of multi-walled carbon nanotubes and titanium dioxide. *J. Colloid. Interface. Sci.* **2012**, *371*, 101–106. [CrossRef] [PubMed]

81. Chen, H.; Motuzas, J.; Martens, W.; da Costa, J.C.D. Degradation of azo dye Orange II under dark ambient conditions by calcium strontium copper perovskite. *Appl. Catal B Environ.* **2018**, *221*, 691–700. [CrossRef]

82. Zubir, N.A.; Yacou, C.; Motuzas, J.; Zhang, X.; Zhao, X.S.; da Costa, J.C.D. The sacrificial role of graphene oxide in stabilising a Fenton-like catalyst GO–Fe$_3$O$_4$. *Chem. Commun.* **2015**, *51*, 9291–9293. [CrossRef] [PubMed]

83. Zheng, J.; Gao, Z.; He, H.; Yang, S.; Sun, C. Efficient degradation of Acid Orange 7 in aqueous solution by iron ore tailing Fenton-like process. *Chemosphere* **2016**, *150*, 40–48. [CrossRef]

84. Liang, X.; Zhong, Y.; Zhu, S.; Zhu, J.; Yuan, P.; He, H.; Zhang, J. The decolorization of Acid Orange II in non-homogeneous Fenton reaction catalyzed by natural vanadium–titanium magnetite. *J. Hazard. Mater.* **2010**, *181*, 112–120. [CrossRef]

85. Leiw, M.Y.; Guai, G.H.; Wang, X.; Tse, M.S.; Ng, C.M.; Tan, O.K. Dark ambient degradation of Bisphenol A and Acid Orange 8 as organic pollutants by perovskite SrFeO3− δ metal oxide. *J. Hazard. Mater.* **2013**, *260*, 1–8. [CrossRef] [PubMed]

86. Sun, M.; Jiang, Y.; Li, F.; Xia, M.; Xue, B.; Liu, D. Structure, dye degradation activity and stability of oxygen defective BaFeO3− x. *Mater. Trans.* **2010**, *51*(11), 1981–1989. [CrossRef]

87. Wei, S.; Hu, X.; Liu, H.; Wang, Q.; He, C. Rapid degradation of Congo red by molecularly imprinted polypyrrole-coated magnetic TiO_2 nanoparticles in dark at ambient conditions. *J. Hazard. Mater.* **2015**, *294*, 168–176. [CrossRef] [PubMed]

88. Momenia, M.M.; Nazari, Z. Preparation of TiO_2 and WO3–TiO_2 nanotubes decorated with PbO nanoparticles by chemical bath deposition process: A stable and efficient photo catalyst. *Ceramics Int.* **2016**, *42*, 8691–8697. [CrossRef]

89. Wang, P.; Qi, C.; Wen, P.; Hao, L.; Xu, X.; Agathopoulos, S. Synthesis of Si, N co-Doped Nano-Sized TiO_2 with High Thermal Stability and Photocatalytic Activity by Mechanochemical Method. *Nanomaterials* **2018**, *8*, 294. [CrossRef] [PubMed]

90. Uddin, M.T.; Babot, O.; Thomas, L.; Olivier, C.; Redaelli, M.; D'Arienzo, M.; . Toupance, T. New insights into the photocatalytic properties of RuO_2/TiO_2 mesoporous heterostructures for hydrogen production and organic pollutant photodecomposition. *J. Phys. Chem. C* **2015**, *119*, 7006–7015. [CrossRef]

91. Li, P.; Song, Y.; Wang, S.; Tao, Z.; Yu, S.; Liu, Y. Enhanced decolorization of methyl orange using zero-valent copper nanoparticles under assistance of hydrodynamic cavitation. *Ultrason. Sonochem.* **2015**, *22*, 132–138. [CrossRef] [PubMed]

92. Shen, T.; Jiang, C.; Wang, C.; Sun, J.; Wang, X.; Li, X. A TiO_2 modified abiotic–biotic process for the degradation of the azo dye methyl orange. *RSC. Adv.* **2015**, *5*, 58704–58712. [CrossRef]

93. Parshetti, G.K.; Telke, A.A.; Kalyani, D.C.; Govindwar, S.P. Decolorization and detoxification of sulfonated azo dye methyl orange by Kocuria rosea MTCC 1532. *J. Hazard. Mater.* **2010**, *176*, 503–509. [CrossRef] [PubMed]

94. Babushkina, M.S.; Nikitina, L.P.; Goncharov, A.G.; Ponomareva, N.I. Water in the structure of minerals from mantle peridotites as controlled bythermal and redox conditions in the upper mantle. *Geol. Ore Deposits.* **2009**, *51*, 712–722. [CrossRef]

95. Garand, E.; Wende, T.; Goebbert, D.J.; Bergmann, R.; Meijer, G.; Neumark, D.M.; Asmis, K.R. Infrared spectroscopy of hydrated bicarbonate anion clusters: HCO_3−(H_2O)1−10. *J. Am. Chem. Soc.* **2009**, *132*, 849–856. [CrossRef] [PubMed]

96. Ge, L.; Han, C.; Liu, J. Novel visible light-induced g-C_3N_4/Bi_2WO_6 composite photocatalysts for efficient degradation of methyl orange. *Appl. Catal B Environ.* **2011**, *108*, 100–107. [CrossRef]